JOINT INSTITUTE FOR NUCLEAR RESEARCH

November 26, 2018

Conceptual and technical design of the Spin Physics Detector (SPD) at the NICA collider

Contents

1 Executive summary **3**

2 Physics case **7**

2.1 Studies of the nucleon and light nuclei spin structure via measurements of Non-Perturbative Quantum Chromodynamics distributions . . . 7

2.2 MMT-DY pair production . . . 8

2.3 Prompt photon production . . . 10

2.4 Charmonium production . . . 13

2.4.1 TMD PDFs in J/ψ production . . . 14

2.4.2 Exotic charmonium states . . . 14

2.5 Generalized parton distributions . . . 15

3 Polarized beams **18**

3.1 Available species and types of collisions . . . 18

3.2 Beam structure, intensity and luminosity . . . 18

3.3 Polarization degree, control and monitoring . . . 19

4 Detector setup **20**

4.1 General design . . . 20

4.2 Magnetic system . . . 20

4.3 Vertex detector (inner tracker) . . . 22

4.3.1 Overview . . . 22

4.4 Main tracker . . . 24

4.5 Electromagnetic calorimeter . . . 26

4.6 Range System . . . 26

4.6.1 General description . . . 26

4.6.2 System layout . . . 27

4.6.3 Mini drift tubes . . . 28

4.6.4 Performance . . . 29

4.7 Particle Identification System . . . 29

4.7.1 SPD ToF system . . . 29

4.8 T0 counter . . . 30

4.9 System for local polarimetry . . . 31

4.9.1 Asymmetry in inclusive production of charged particles . . . 31

4.9.2 Single transverse spin asymmetry for very forward neutron production 32
4.9.3 Inclusive $pp \to \pi^0 X$ reaction 32
4.10 Data acquisition system and slow control 33

5 Beam test facility **36**

6 Integration and Services. **38**
6.1 Service systems 38

7 Software design and computing **40**
7.1 SPDroot 40

8 MC simulation and physics performance **41**
8.1 Rates and spectra for minimum bias events 41
8.2 Rates, spectra, background, etc. for processes of interest 41
8.2.1 Drell-Yan pair production 41
8.2.2 Physics with prompt photons 41
8.2.2.1 Signal and background 41
8.2.2.2 Performance requirements for the SPD setup 42
8.2.2.3 Expected accuracy for asymmetries A_N and A_{LL} 42
8.2.3 Charmonia reconstruction 43
8.2.3.1 Kinematic distributions, reconstruction efficiency and expected statistics 43
8.2.3.2 Expected background 44

9 Participating institutions and author list **50**

10 Project time-line **52**

1 Executive summary

Since the famous "spin crisis" that began in 1987, the problem of the nucleon spin structure remains one of the most intriguing puzzles in the contemporary high-energy physics. The central component of this problem, attracting for many years enormous both theoretical and experimental efforts, is the problem how the spin of the nucleon is built up from spins and orbital momenta of its constituents. The searches brought up a concept of the spin-dependent parton distribution functions of the nucleon, at the beginning only two were proposed: f_1 for unpolarized and g_1 for polarized nucleons. Now we know that there must be of about 50 different parton distribution functions for a complete description of the nucleon structure. While today a part of the polarized distributions can be considered as sufficiently well known, there is a number of PDFs that either are absolutely unknown, or poorly known, especially the spin dependent ones.

The composite nature of the nucleon spin structure has been studied for a long time by means of deep inelastic scattering (DIS) of leptons and production of Drell-Yan (DY) [1, 2] lepton pairs. In a regime of a large momentum transfer Q the scattering occurs in a collinear configuration between the incident lepton and a single parton in the nucleon (the so called Bjorken regime). A factorization theorem exists [3–6] that allows us to express the inclusive DIS and DY cross sections as a convolution of two contributions: one that corresponds to the hard process occurring at a short distance between the probe and the parton; and another one that accounts for the coherent long-distance interactions between the struck parton and the target, and is described in terms of parton distributions.

At leading order (leading twist, LO) the Bjorken variable x can be interpreted as the fraction of the longitudinal momentum of the parent (fast-moving) nucleon carried by the active parton, and one may distinguish three kinds of parton distributions functions (PDF). Two of them are well-known structure functions measured in DIS and other processes: $f_1^a(x)$ (a is a parton flavor, often suppressed) is the density of unpolarized partons with longitudinal momentum fraction x in an unpolarized nucleon, and $g_1(x)$ giving the net helicity of partons in a longitudinally polarized nucleon. The third one, the transversity $h_1(x)$, describing the density of partons with polarization parallel to that of a transversely polarized nucleon minus the density of partons with antiparallel polarization, is chiral-odd and requires a quark helicity flip in the scattering that cannot be achieved in the hard subprocess. Other parts of the cross section have to be explored for that. They are either chiral-odd fragmentation functions (FF) (e.g. Collins fragmentation function $H_1^\perp(x)$ in semi inclusive DIS (SIDIS)) or yet another transversity, that of the second polarized incident hadron in the DY.

However, in addition to the information on the longitudinal behaviour in momentum space along the direction in which the nucleon is moving, drawing a complete three-dimensional picture of the nucleon also requires knowledge of the transverse motion of the partons [7, 8]. A full account of the orbital motion, which is also an important issue to understand the spin structure of the nucleon, can be given in terms of transverse-momentum dependent parton distribution functions (TMDs). There are eight leading-twist TMDs: $f_1(x,p_T)$, $f_1^\perp(x,p_T)$, $g_{1L}(x,p_T)$, $g_{1T}(x,p_T)$, $h_1(x,p_T)$, $h_{1L}^\perp(x,p_T)$, $h_{1T}^\perp(x,p_T)$ and $h_1^\perp(x,p_T)$ [9].

Two of them, the Boer-Mulders and Sivers functions, $h_1^\perp(x,p_T)$ and $h_{1T}^\perp(x,p_T)$ [9–11], are T-odd, i.e. they change sign under naive time reversal, which is defined as usual time reversal, but without interchange of initial and final states. The other six leading-twist TMDs are T-even.

In order to be sensitive to intrinsic transverse parton momenta, it is necessary to measure the transverse momenta of the produced hadrons in the final state, e.g., in processes like semi-inclusive lepton-nucleon DIS (SIDIS), hadron production in e^+e^- annihilation [7] or the transverse momentum of the lepton pair in the Drell-Yan processes in hadron-hadron collisions. Here, factorization has been proven at leading twist [12–15] allowing to get information about TMDs as well as on fragmentation functions (FFs) describing the hadronization process of the hit quark into the detected hadrons.

By measuring the angular distribution of produced hadrons in SIDIS or lepton pairs in DY, it is possible to obtain information about all the eight leading-twist TMDs in combinations with the two leading-twist FFs.

According to the factorization theorem, each of the leading-twist structure functions can be conceived as a convolution between one TMD and one FF in SIDIS or two TMDs (for the quark and antiquark) in the DY. Since the structure functions enter the cross section with a defined angular coefficient, they can be accessed by looking at specific azimuthal asymmetries. This has become now a powerful tool for studying the three-dimensional structure of the nucleon and many more data are expected to come in the future. The remarkable experimental progress was motivated and accompanied by numerous theoretical and phenomenological studies.

During the past decades, dilepton production in high-energy hadron-hadron collisions played an important role in order to pin down parton distributions (PDFs) of hadrons. While the focus was on PDFs of the nucleon, also information on the partonic structure of the pion was obtained through Drell-Yan measurements. Experimentally, the Drell-Yan process is quite challenging because of the relatively low counting rates. On the other hand, from the theoretical point of view it is the cleanest hard hadron-hadron scattering process. The fact that there is no need to detect hadrons in the final state simplifies the proof of factorization in comparison to hadron-hadron collisions with hadronic final states. This important point is one of the main reasons for the continued interest in the Drell-Yan reaction in hadron-hadron collisions.

Currently, not less than six programs for future Drell-Yan measurements are pursued. These plans comprise dilepton production in nucleon-nucleon collisions (at RHIC [16], J-PARC (KEK) [17, 18], IHEP (Protvino) [19], and at the JINR (Dubna) [20, 21], in antiproton nucleon collisions (at FAIR (GSI) [22], as well as in pion nucleon collisions (at COMPASS (CERN) [23]. Past measurements exclusively considered measurements of the unpolarized cross section, but all future programs are also aiming at polarization measurements. Including polarization of the incoming hadrons opens up a variety of new opportunities for studying the strong interaction in both the perturbative and the non-perturbative regime.

The objective of the proposed experiment is also the study of the gluon structure of the nucleon. It is of fundamental importance as it is needed to understand the nucleon internal structure as a whole. The unpolarized gluon content of the proton is well-known while our knowledge of polarized parton distributions (including TMDs) is limited.

There are two main hard processes for the production of direct photons: gluon Compton scattering, $gq(\bar{q}) \to \gamma q(\bar{q})$, which dominates and gives access to the gluon distributions in the nucleon, and quark-antiquark annihilation, $q\bar{q} \to \gamma g$. The contribution of the latter process to the total cross section presumably does not exceed 20%. A few fixed-target and collider experiments performed unpolarized measurements of the prompt-photon production differential cross section [24]. A certain tension between data of the fixed-target results, the collider ones and the theoretical expectations takes place. New precise measurements could clarify the issue.

Measurement of single transverse spin asymmetry in prompt-photon production at high p_T in polarized p-p and d-d collisions could provide information about the gluon Sivers function, which is the mostly unknown function at the moment [25]. In general, the investigation of processes with prompt photons, as well as charmonium production is a proven way to enhance the available rather scarce experimental information on the gluon content of the hadrons.

The opportunity to have high luminosity collisions of polarized protons and deuterons at the NICA collider allows for studies of a great variety of spin and polarization dependent effects in the hadron-hadron collisions:

– Drell-Yan (DY) pair production and prompt-photon processes with longitudinally and transversely

polarized p and d beams. Extraction of unknown (poor known) parton distribution functions (PDFs) from J/ψ production processes and spin effects in baryon, meson and photon production;

- different effects in various exclusive reactions;
- diffractive processes;
- cross sections, helicity amplitudes and double spin asymmetries (Krisch effect) in elastic reactions;
- spectroscopy of quarkonia.

The principal aim of this proposal is to elaborate a design concept for a detector (Spin Physics Detector, SPD) capable to exploit the broad spin physics potential of the NICA collider. The physics program, requirements for the detector and the design ideas are based on the submitted in 2014 Letter of Intent [21] that was endorsed by the JINR Pphysics Advisory Committee (PAC) for Particle Physics .

The SPD facility is foreseen to be allocated in the south beam interaction point of the NICA collider.

The requirements for the detector are listed below:

- close to 4 geometry for secondary particles;
- high-precision ($\sim 50\mu m$) and fast vertex detector;
- high-precision ($\sim 100\mu m$) and fast tracking system;
- precision momentum measurement of secondary particles;
- good particle identification capabilities ($e^{\pm}, \pi^{\pm}, K^{\pm}, \mu^{\pm}, p^{\pm}$ etc.);
- efficient muon range system;
- good electromagnetic calorimeter;
- low material budget over the track paths;
- trigger and DAQ system able to cope with event rates at luminosity of 10^{32} cm^{-2}s^{-1};
- modularity and easy access to the detector elements in view of reconfiguration and further upgrade of the facility.

The aim is to have yet simple but universal detector that could be relatively easily reconfigured and/or upgraded.

The detector consists of three modules: two end-caps and a barrel section. Each part has an individual magnet system: the endcaps - solenoidal coils, the barrel - toroidal magnetic system. The main detector systems are as follows: Range System (for muon identification), Electromagnetic Calorimeter, PID/Time-of-Flight system, Main Tracker and Vertex Detector. The proposed three-module design gives a possibility for upgrade and modification of each of the main detector subsystems and for performing measurements in different detector configurations.

Preliminary MC simulations have been carried out in order to evaluate the capabilities of such a system to perform the foreseen measurements. The results are encouraging.

The current project includes as a component design and construction of a SPD test zone at one of the extracted beams of the Nuclotron for testing of the detector prototypes in beams of various particle species and of different momenta in the energy range of interest.

Host institute of the project is the Laboratory of High-Energy Physics of the Joint Institute for Nuclear Research. The main part of the human resources engaged with the project comes from there (74 researchers, 24.4 FTE). The Laboratory of Nuclear Problems is the other laboratory of the JINR that participates in the project with substantial number of researchers (30 researchers, 11.3 FTE). Altogether the JINR engagement in the project now evaluates to 37.7 full-time-equivalent (FTE) researchers.

Fourteen institutes from the JINR Member States and other countries have expressed by now their interest for participation in the project and indicate that they could allocate resources and manpower for the project.

We propose a five-year project for delivering of a complete technical design of the SPD facility based on the necessary simulation work, prototypes construction and test measurements.

The time-line is seen as follows:

- submission of a JINR project for design of the SPD facility for the PAC meeting in January 2019;
- setting up of the SPD collaboration and election of its management bodies (2019);
- signing of MoU (2019);
- preparation of Conceptual Design Report and submission to the PAC by the end of 2019;
- preparation of Technical Design Report for the first stage of the facility, including prototyping and test measurements (2020 - 2022);
- preparation of Technical Design Report for the second stage (2023).

We hope to be able to start construction of the first stage of the detector in 2022 and perform first measurements somewhere in 2025.

2 Physics case

2.1 Studies of the nucleon and light nuclei spin structure via measurements of Non-Perturbative Quantum Chromodynamics distributions

The Quantum Chromodynamics (QCD) is the only part of the Standard Model that exhibits fully non-perturbative (NP) behaviour. In this respect it is similar to the rich and complicated phenomena in condensed matter physics, hydrodynamics, plasma physics, astrophysics, etc.

Important information about the non-perturbative QCD is provided by various collective phenomena emerging in heavy-ion collisions that will be studied at BM@N and MPD detectors at the NICA complex.

The SPD project will follow a complementary way for investigating of the non-perturbative QCD phenomena, namely by exploration of the nucleon structure. In modern terms, the latter is described by a vast set of various parton distributions and correlations. The most general of them is the (”mother”) Wigner function, containing the full information about the longitudinal and transverse spin and momentum partonic degrees of freedom. The average over some variables or putting some others to particular (zero) values leads to more simple and more easily measurable description of the fundamental particles, quarks and gluons, inside hadrons. An important stage of this reduction process is represented by a set of Transverse-Momentum-Dependent Parton Distributions (TMDs) and the process ends when the familiar collinear parton distributions appear.

The SPD project provides a unique opportunity for studies of various elements of the hadron structure in one and the same experiment. It opens a possibility of comparative studies of observables (especially spin effects) in collisions of hadrons and light nuclei, which, in turn, may be compared to the data on heavy-ion collisions from the MPD and BM@N. It offers also a complementary look to the same functions studied in lepton-hadron scattering, benefitting from the overlapping energy range of the SPD and COMPASS and, partially, JLab. The core of these investigations is formed by studies of spin-dependent and spin-independent TMDs.

Usually, the exploration of Parton Distributions is based on some sort of Factorisation Theorem (which in various cases is proved with different degree of rigour) when the short-distance part of the process described by the Perturbative QCD (utilising the Asymptotic Freedom) is used as a sort of ”microscope” to probe the non-perturbative parts. SPD will use several such microscopes.

The most clean process is the production of massive lepton pairs discovered by Drell and Yan (DY) and, independently, at JINR, by Matveev, Muradyan and Tavkhelidze (MMT). The MMT-DY process with one transverse polarized hadron allows us to measure the full set of leading TMDs.

The measurement of TMDs requires to measure the angular distribution of the lepton pair in its c.m. frame that gives access to the tensor polarization of the virtual photon. Such a measurement is of major importance even in unpolarized collisions, being the probe of various aspects of the hadron structure, e.g. T-odd Boer-Mulders function, via the deviation from the so-called Lam-Tung relation.

The average transverse momentum of the MMT-DY pairs provides information about twist-3 ETQS quark-gluon correlators discovered in JINR by Efremov and Teryaev (fermionic poles) and by Qiu and Sterman (gluonic poles). The transverse twist-3 asymmetry in the MMT-DY process allows one to measure the gluonic pole correlator and test its normalization, where the latter receives extra factor 2 from subtle QCD effect discovered recently in JINR.

The MMT-DY process with polarized deuteron beam allows one to measure the tensor parton distribution that is related to the quark gravitational form factors. These form factors got recently much attention due to the experimental observation of pressure inside the proton.

The production of exclusive MMT-DY pairs also provide an access to other important objects - General-

ized Parton Distributions, in particular to those related to the recently measured pressure of quarks in the proton.

Another process ("microscope") sensitive to TMDs is the J/Ψ production. In the case of $q\bar{q}$ anihilation there is a duality to the MMT-DY process (known also as fusion model) so that the J/Ψ production gives the same information as MMT-DY itself, being experimentally less demanding measurement.

Yet another process, sensitive to TMDs, is the direct photon production. It provides direct access to various gluon TMDs.

The production of hadrons with large transverse momentum, contrary to MMT-DY and direct photon production, brings up a necessity of taking into account the fragmentation process. At the same time, the larger cross sections allow for more accurate measurements. Performing measurements of transverse single spin asymmetries over certain range in rapidity and transverse momentum will make possible a scan of the twist-3 correlators. This scan may be complemented with similar studies in lepton-hadron scattering by COMPASS and in JLab.

Large transverse momentum production also allows one to search for multiquark and exotic states, as well as to consider processes probing the cold nuclear matter complementary to searches of the short range correlations at BM@N.

While the SPD main target is hadronic collisions, the ultraperipheral nuclear scattering may be also accessible. In proton-nuclei collisions such an object like the nucleus Wigner function may be measured.

In general, the SPD physics program is aimed at measurements of various non-perturbative QCD functions, describing the structure of the nucleon. The main features of the program are listed below:

- measurement of various TMDs in the same experiment;
- comparison of results for hadronic and light nuclei collisions that may be confronted with the MPD data for heavy-ion collisions;
- complementarity to the lepton-hadron measurements.

2.2 MMT-DY pair production

Parton Distribution Functions (PDFs) describe the structure of the nucleon in terms of the nucleon momentum fraction carried by a parton. They have been generalized to contain information not only for the longitudinal but also for the transverse distributions of the partons in a fast moving hadron, resulting in a theoretical framework of the "3-dimensional picture" (3D) of the nucleon called "nucleon tomography". In addition, effects of the intrinsic transverse motion of the partons are described via so-called Transverse-Momentum-Dependent PDFs (TMDs). These effects are experimentally investigated by studying the Drell-Yan (DY) processes in collisions of unpolarized and polarized beams.

Eight independent parton distributions are needed, in the leading twist approximation, to describe the nucleon structure in terms of longitudinal and transverse spatial and momentum parton distributions, see Figure 1. These distributions are probed experimentally by measuring of specific azimuthal asymmetries, listed below.

1. Transversity: $A_{UT}^{\sin(\phi+\phi_S)}$, represents the number distribution of transversely polarized quarks in a transversely polarized nucleon;
2. Sivers: $A_{UT}^{\sin(\phi-\phi_S)}$, represents the distribution over the transverse momentum of non-polarized quarks in a transversely polarized nucleon;

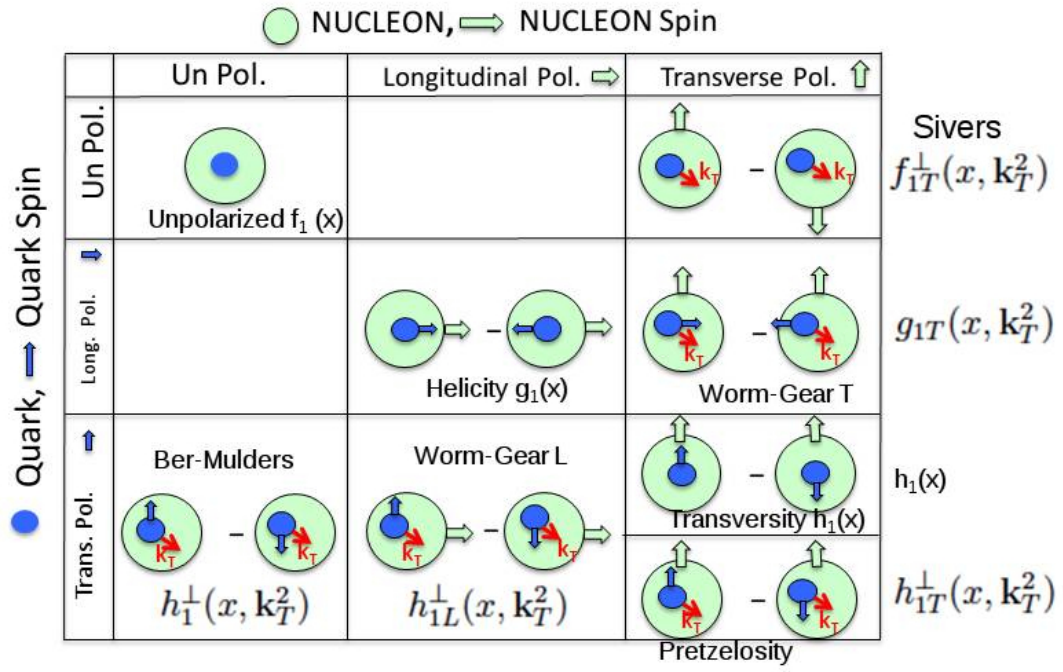

Figure 1: Leading twist TMD distribution functions. The U,L,T correspond to unpolarized, longitudinally polarized and transversely polarized nucleons (rows) and quarks (columns).

3. Pretzelosity: $A_{UT}^{\sin(3\phi-\phi_S)}$, represents the distribution over the transverse momentum of transversely polarized quarks in a transversely polarized nucleon;

4. Boer-Mulders: $A_{UU}^{\cos(2\phi_h)}$, represents the distribution over the transverse momentum of transversely polarized quarks in a non-polarized nucleon;

5. Worm-Gears: $A_{UL}^{\cos(2\phi_h)}$, represents the distribution over the transverse momentum of longitudinally polarized quarks in a longitudinally polarized nucleon.

All the asymmetries and respective PDFs could be measured by the Spin Physics Detector, in one and the same set-up, thus largely minimizing the systematic uncertainties [21].

Two approaches could be used the extract different PDFs (see section 2 of [21]). The first one is a Fourier analysis of the measured azimuthal asymmetries [26–32], and the second one is via studying of integrated/weighted asymmetries [20, 33–36]. For example, theoretical estimation of the Sivers asymmetry is given in Figure 2. Three different functions for the Sivers distributions are used to estimate the asymmetries in Figure 2: curves I and II are taken from [37] and the last one, denoted as fit III, is from [38].

Some predictions for the Boer-Mulders asymmetries are given in Figure 3.

For the moment, only the COMPASS collaboration has published experimental results from measurements of the Drell-Yang processes in hadron-hadron interactions, using the CERN SPS 190 GeV/c π^- beam and a transversely polarized ammonia target [39]. Three experimentally measured azimuthal asymmetries giving access to different TMDs parton distribution functions are presented in Figure 4.

The SPD experiment would give comparable and even more precise data on these and other asymmetries of interest.

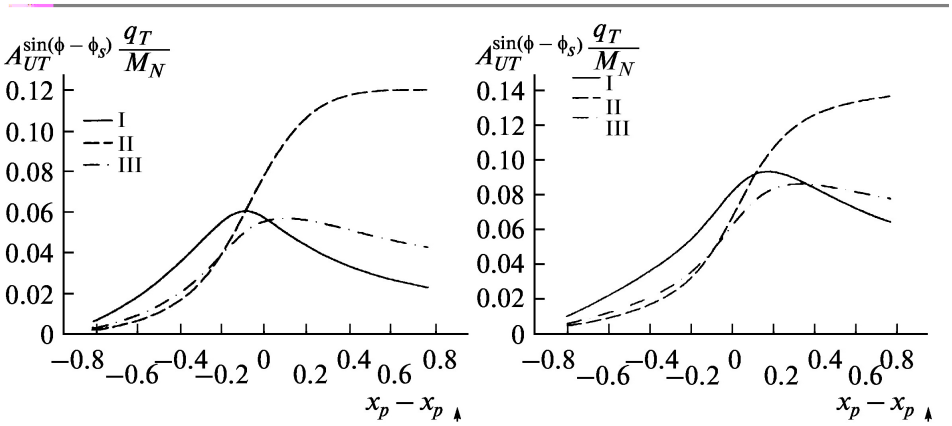

Figure 2: Estimated Sivers asymmetries for NICA conditions, $s = 400GeV^2$, $Q^2 = 4Gev^2$ (left panel). and $15GeV^2$ (right panel) (details are given in text).

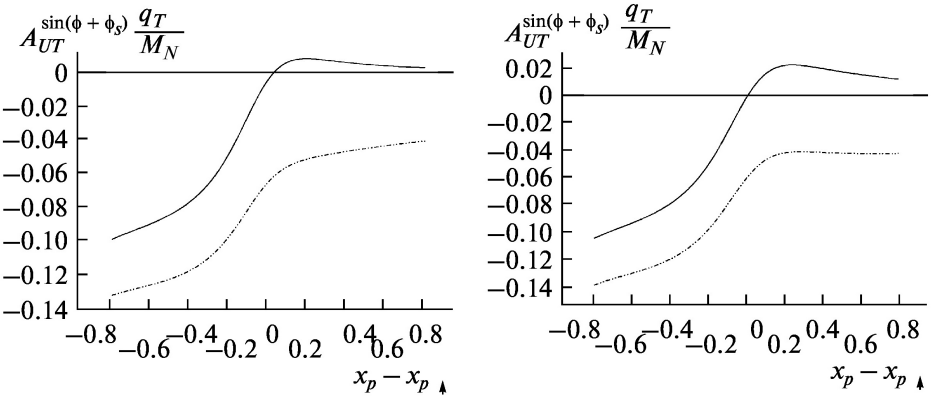

Figure 3: Estimated Boer-Mulders asymmetries for NICA conditions.

2.3 Prompt photon production

Prompt photons are photons that are produced by hard scattering of partons. According to the factorization theorem, the inclusive cross section for the production of a prompt photon in a collision of hadrons h_A and h_B can be written as follows:

$$d\sigma_{AB\to\gamma X} = d\sigma_{dir} + d\sigma_{frag} = \sum_{a,b=q,\bar{q},g} \int dx_a dx_b f_a^A(x_a,Q^2) f_b^B(x_b,\mu^2) d\sigma_{ab\to\gamma x}(x_a,x_b,Q^2) + d\sigma_{frag}. \quad (1)$$

Here, $d\sigma_{dir}$ is the contribution of photons emitted via direct coupling to a quark (direct photons) and $d\sigma_{frag}$ represents the contribution of photons produced from the fragmentation of a final partonic state (fragmentation photons). The function f_a^A (f_b^B) is the parton density for hadron h_A (h_B), x_a (x_b) is the fraction of the momentum of hadron h_A (h_B) carried by parton a (b) and Q^2 is the square of the 4-momentum transferred in the hard scattering process, and $\sigma_{ab\to\gamma x}(x_a,x_b,Q^2)$ represents the cross section for the hard scattering of partons a and b. Prompt photon production in hadron collisions is the most direct way to access the gluon structure of hadrons.

There are two main hard processes for the production of direct photons: i) gluon Compton scattering, $gq(\bar{q}) \to \gamma q(\bar{q})$, which dominates, and ii) quark-antiquark annihilation, $q\bar{q} \to \gamma g$. Contribution of the latter process to the total cross section presumably does not exceed 20% .

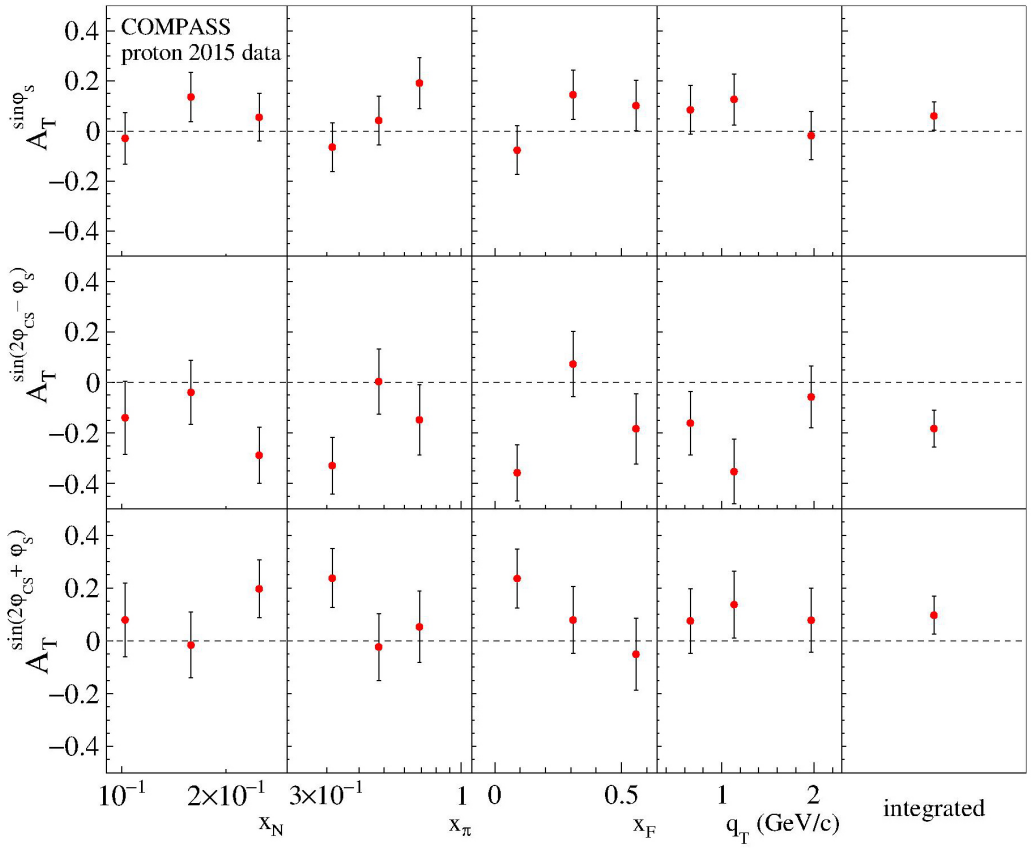

Figure 4: COMPASS data on Drell–Yan pair production spin asymmetries related to Sivers, transversity and pretzelosity TMD PDFs (top to bottom).

A few fixed-target and collider experiments performed unpolarized measurements of the prompt-photon production differential cross section. Figure 5 shows the ratio of the measured cross sections to the theoretically predicted one as a function of the $x_T = 2p_t/\sqrt{s}$ [24]. One can see that the fixed-target results ($\sqrt{s} \sim 20$ GeV) disagree significantly with the theoretical expectations while this is not the case for the collider results. New precise measurements could clarify the puzzle.

Measurement of single transverse spin asymmetry A_N^γ in prompt-photon production at high p_T in polarized p-p and d-d collisions could provide information about the gluon Sivers function which is the mostly unknown function at the moment [25]. The numerator of A_N^γ can be expressed as [40]

$$\sigma^\uparrow - \sigma^\downarrow = \sum_i \int_{x_{min}}^1 dx_a \int d^2\mathbf{k}_{Ta} d^2\mathbf{k}_{Tb} \frac{x_a x_b}{x_a - (p_T/\sqrt{s})\, e^y} \left[q_i(x_a, \mathbf{k}_{Ta}) \Delta_N G(x_b, \mathbf{k}_{Tb}) \times \frac{d\hat{\sigma}}{d\hat{t}}(q_i G \to q_i \gamma) + G(x_a, \mathbf{k}_{Ta}) \Delta_N q_i(x_b, \mathbf{k}_{Tb}) \frac{d\hat{\sigma}}{d\hat{t}}(G q_i \to q_i \gamma) \right] . \quad (2)$$

Here $\sigma^\uparrow$ and $\sigma^\downarrow$ are the cross sections of the direct photon production for the opposite transverse polarizations of one of the colliding protons, $q_i(x, \mathbf{k}_{Ta})$ $[G(x, \mathbf{k}_{Ta})]$ is the quark [gluon] distribution function with specified $\mathbf{k}_T$ and $\Delta_N G(x_b, \mathbf{k}_{Tb})$ $[\Delta_N q_i(x_b, \mathbf{k}_{Tb})]$ is the gluon [quark] Sivers function. $d\hat{\sigma}/d\hat{t}$ represents corresponding gluon Compton scattering cross section. Authors of the work [41] pointed out that the asymmetry A_N^γ at large positive x_F is dominated by quark-gluon correlations while at large negative x_F it is dominated by pure gluon-gluon correlations as it was concluded in [42]. Further development of the corresponding formalism can be found in [43, 44]. It is important to notice that the corresponding known to be non-zero asymmetry in π^0 production, $A_N^{\pi^0}$ [], could be accessed in the same measurements.

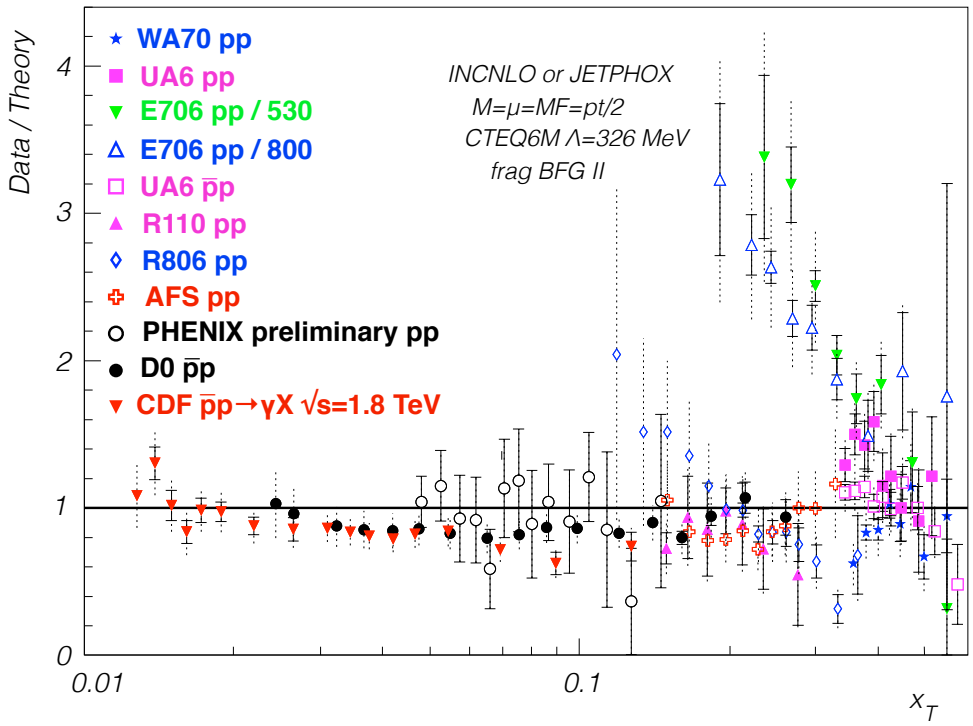

Figure 5: Measured cross section of prompt-photon production divided by the predicted one as a function of the x_T [24].

The first attempt to measure A_N^γ at $\sqrt{s} = 19.4$ GeV was performed in the fixed target experiment E704 at Fermilab in the kinematic range $-0.15 < x_F < 0.15$ and 2.5 GeV/c $< p_T <$ 3.1 GeV/c. The results were consistent with zero within large statistical and systematic uncertainties [45].

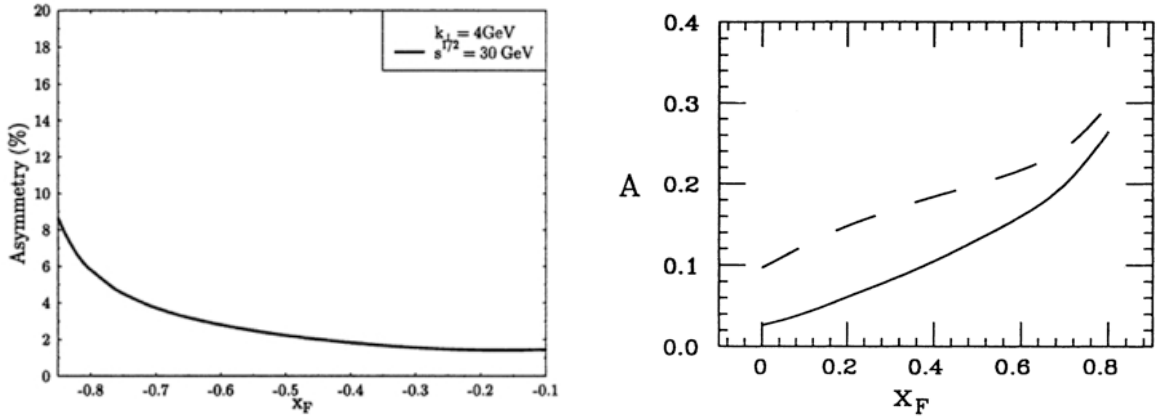

(a) (b)

Figure 6: Theoretical predictions for A_N^γ at $\sqrt{s} = 30$ GeV and $p_T = 4$ GeV/c for (a) positive [43] and (b) negative [41] values of x_F.

Study of prompt-photon production at large transverse momenta with longitudinally polarised proton beams could provide access to gluon polarisation Δg via measurement of the longitudinal double spin asymmetry A_{LL}^γ [46]. Assuming a dominance of the gluon Compton scattering process, the asymmetry

A_{LL}^{γ} can be presented as [47]

$$A_{LL} \approx \frac{\Delta g(x_a)}{g(x_a)} \cdot \left[\frac{\sum_q e_q^2 [\Delta q(x_b) + \Delta \bar{q}(x_b)]}{\sum_q e_q^2 [q(x_b) + \bar{q}(x_b)]} \right] \cdot \hat{a}_{LL}(gq \to \gamma q) + (a \leftrightarrow b)\,. \tag{3}$$

The second factor in the equation coincides, to the lowest order, with the spin asymmetry A_1^p well-known from polarised DIS, while the partonic asymmetry $\hat{a}_{LL}$ is calculable in the perturbative QCD. Previous results for the gluon polarization show that it is consistent with zero: $|\Delta g/g| < \pm 0.2$, while the asymmetry A_1^p is of about 0.2. Thus, it seems that the value of A_{LL}^{γ} should not exceed a few per cent level. Measurement of A_{LL}^{γ} asymmetry as well as A_N^{γ} is part of the spin physics programme at the RHIC collider [].

In addition, in some papers [48, 49] it is proposed to pay attention to associative prompt-photon production in reactions like $pp \to \gamma J/\psi X$.

2.4 Charmonium production

The J/ψ (and charmonium in general) production in hadron collisions is of great interest for several reasons. Firstly, the description of the process is a challenge and an important test for our understanding of the QCD. Despite of the considerable efforts that have been devoted to study charmonium production since the J/ψ discovery and the existence of several theoretical approaches to the problem, no fully consistent understanding of the process has been obtained yet. Secondly, comprehensive understanding of the charmonium production process would allow one to separate the quark-antiquark annihilation and gluon-gluon fusion contributions, and thus to benefit from large (compared to the Drell-Yann process) statistics of inclusive J/ψ events to measure and interpret transverse spin asymmetries. Thirdly, the production process is sensitive to the gluon content of the colliding hadrons, while experimentally J/ψ can be easily reconstructed from the very clean dilepton modes, making it a powerful tool to probe gluon parton distribution functions. This is of special interest for the pion and kaon, since the gluon PDF of the former is poorly know and gluon PDF of the latter has not been measured yet. It must be noted, that a significant fraction (about 40%) of the J/ψ mesons is produced indirectly through the decays of of χ_{cJ} and $\psi(3686)$ (so called feed-down contributions), thus requiring dedicated study of these charmonium states. All experimental applications of the charmonium production rely on our theoretical understanding of the process. The SPD experiment might be an ideal tool to verify and validate the theoretical approaches at relatively low energies and to obtain related and important physics results.

Reviews on charmonium production mechanisms can be found in Ref. [51, 52].

The two approaches used today are the color evaporation model (CEM) [53], [50], [54]. and the non-relativistic QCD (NRQCD) [55], [56], [57], [52] one. They are usually formulated for collinear factorization of the hadron scattering. In both models formation of a charmonium state goes through color-singlet and color-octet configuration of a $c\bar{c}$ pair. The latter becomes color neutral during formation of the charmonium state by a soft interaction with the collision-induced color field.

Measurement of the differential cross-section with respect to x_F would be a direct tests of the charmonium production models at the SPD energies. In Ref. [50] predictions of the CEM and NRQCD models for collision energies of 15 GeV and 39 GeV are given. The shape and relative contributions of the gluon-gluon fusion and quark-antiquark annihilation are shown in Fig. 7.

The SPD experiment at NICA could provide precise measurements of total cross-section, differential cross-sections with respect to x_F and p_T and polarization for J/ψ. The open geometry of the SPD detector would allow measurements of the same observables for ψ', χ_{c1} and χ_{c2}, that was not possible in the previous fixed-target experiments at the same interaction energy. It must be noted, that analysis of the ψ' production would be much simpler due to the absence of the feed-down contribution. The existing

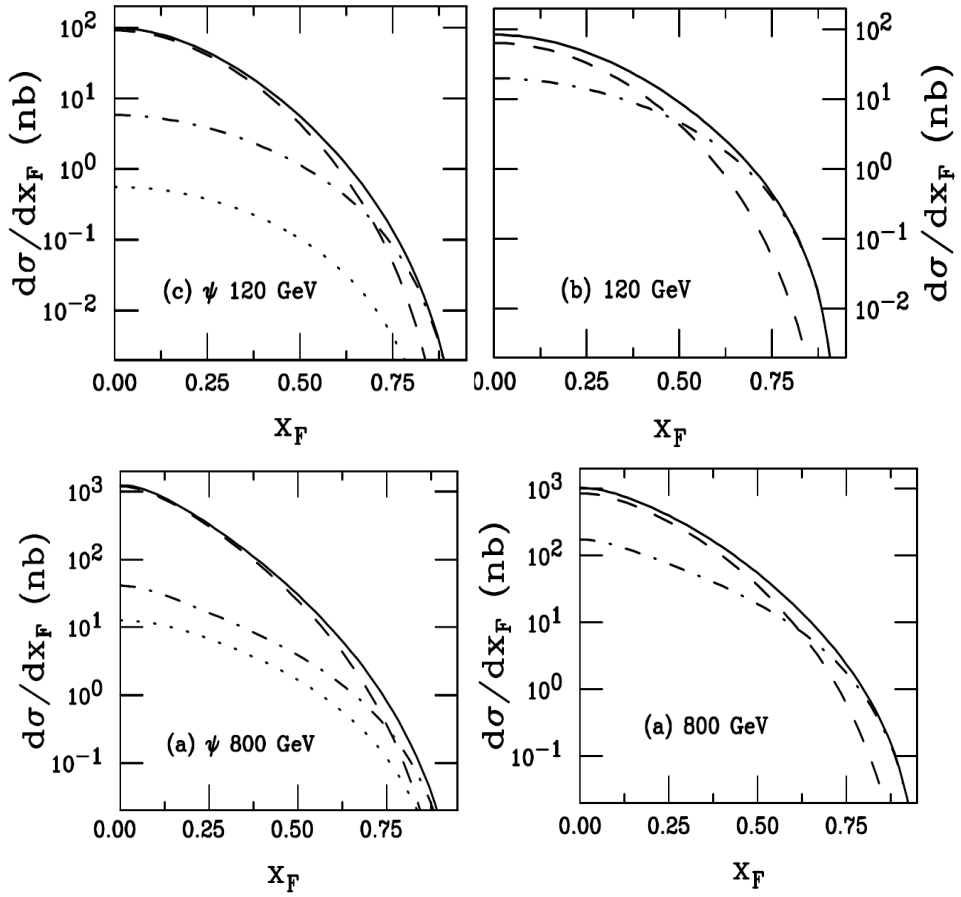

Figure 7: NRQCD (left column) and CEM (right column) predictions for $d\sigma/dx_F$ from Ref. [50] showing contribution from the gluon-gluon fusion (the dashed line) and quark-antiquark annihilation (the dash-and-dotted line) for center-of-mass energies of 15 GeV (top) and 39 GeV (bottom).

experimental data for the total cross section of the J/ψ production in the proton-nucleon collisions at different energies are presented in Figure 8 together with the NRQCD fit. The SPD experiment will cover the most interesting range where, on the one hand, there is discrepancy between the experimental results and, on the other hand, the NRQCD prediction deviates significantly from the data.

2.4.1 TMD PDFs in J/ψ production

The production of lepton pairs in the $q\bar{q}$ annihilation processes via the J/ψ production and its subsequent decay is a process, analogous to the Drell-Yan production mechanism. This analogy is known as the duality model [59, 60]. For the TMD PDF studies, the duality model can predict [61] a similar behavior of the azimuthal asymmetries in the lepton pair's production via Drell-Yan and via the J/ψ leptonic decay. This similarity follows from the idea of the duality model to replace the coupling e_q^2 by the J/ψ vector coupling with $q\bar{q}$ $(g_q^V)^2$ The vector couplings are expected to be the same for u and d quarks [59] and cancel out in the azimuthal asymmetries for large values of x_1 or x_2. For instance we can compare the Sivers asymmetry for Drell-Yan with the corresponding asymmetry for the J/ψ events at different colliding energies.

2.4.2 Exotic charmonium states

The exotic charmonium resonances X, Y, Z, recently observed in some experiments, are among the most mysterious states in the modern particle physics [51],[62], [63], [64].

Studies of their production and decays are planned at many experiments like BESIII at IHEP, LHCb

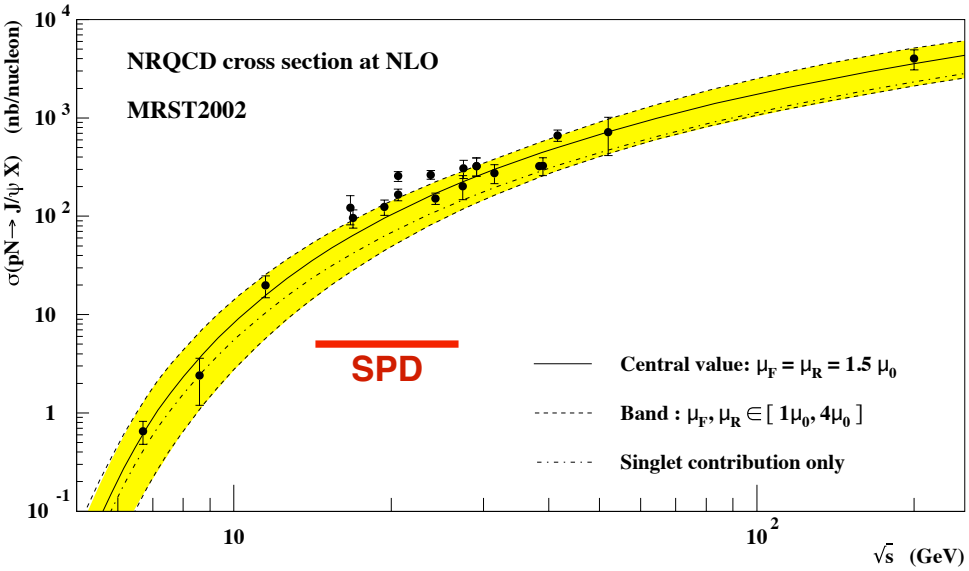

Figure 8: Experimental data for the J/ψ production cross section and the NRQCD fit result [58]. The SPD energy range is shown in red.

at CERN, CDF at Fermilab, PANDA at GSI. The SPD at NICA, in configuration with high-precision vertex detector, would be well suited to observe these states as well as other charmed hadrons in proton-proton and deuteron-deuteron collisions, also in the interesting region above the $D\bar{D}$ threshold. The measurements would shed light on the nature of these exotic states, which are a good test bench for the theories of the strong interactions like perturbative and non-perturbative QCD, Lattice QCD, potential models, phenomenological models, etc.

2.5 Generalized parton distributions

There are several ways to study Generalized Parton Distributions (GPDs), which are important complementary ingredients of hadron structure, at NICA. The respective detector should have a detailed identification of the final particles. In this case it is possible to detect an exclusive reactions like $pp \to ppM$ where M is some meson. The reaction when the proton radiate a photon with small virtuality that interacts with another proton and produce the meson M is shown in Fig. 9(a). In the final state we should observe meson M and two protons.

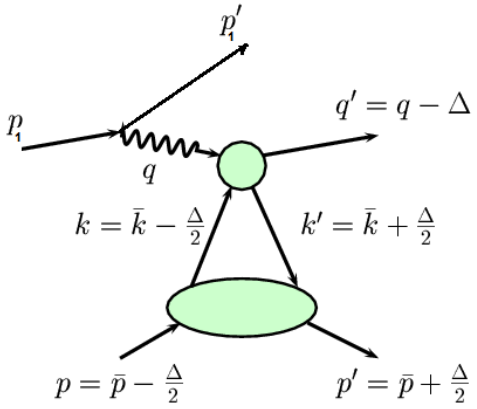

(a)

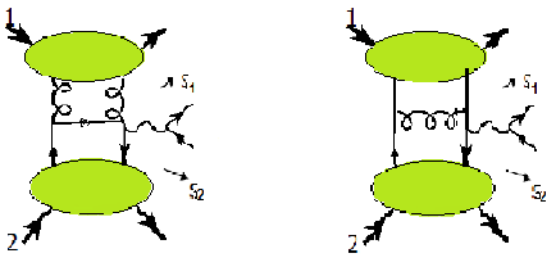

(b)

Figure 9: (a) Vector meson production at NICA via photoproduction mechanism or odderon exchange. (b) Drell-Yan process with gluon and quark GPDs.

At NICA we shall have the energy in the γp system $W = \sqrt{s_2 = (q+p)^2} \sim 5-15$ GeV. The meson photoproduction amplitude can be presented in a factorized form as a convolution of the hard scattering part which can be calculated perturbatively and the Generalized Parton Distributions [65, 66].

This photoproduction contribution is similar to the corresponding process in lepton-proton reaction. However, in the proton-proton reaction we should have in addition to photon exchange a strong interaction contribution. Estimations shows that at NICA the energy $s_1 = (p_1' + q')^2$ is rather large $s_1 \geq 100$ GeV^2. At such energies the gluon contribution should predominate. The minimal number of gluons which can contribute to the Vector Dominance (VD) production process is equal to 3. This exchange can be associated with the odderon contribution. So we shall have at NICA in VM production photon contribution and odderon effects, Figure 9(a). The interference of these effects is of special interest. Generally, the odderon can be effectively regarded as an object similar to the photon. In this case the odderon contribution will be expressed in terms of GPDs as the photoproduction amplitude.

In the ultraperipheral processes one may also study the most general non-perturbative objects, Generalized Transverse Momentum dependent Distributions (GTMD). This possibility was explored at higher energies [67] but the measurements could be also continued to the lower energies of NICA.

One may also consider the ultraperipheral collisions of protons with heavy ions in SPD, which will enhance the photoproduction contribution by several orders of magnitude.

The J/ψ production can be studied at $W \sim 15$ GeV Large meson mass permit to perform perturbative calculation at sufficiently low Q^2. and the photon exchange in J/ψ production should dominate. Cross section in the photon channel is about $\sigma_{J/\psi} \sim 10$ nb. This process is dominated by the gluon GPDs H^g. The $\tilde{H}^g$ effects determined by Δg can be tested in the A_{LL} asymmetry of J/ψ production.

Measurement of exclusive Drell-Yan production in the proton-proton reaction determined by two GPDs contributions was proposed in [68]. This gives possibility to study GPDs at NICA within a exclusive reaction where in the final state we observe two protons and a lepton pair. An example of such a process that contains gluon and quark contribution is shown in Fig. 9(b).

Investigation of the cross section determined by two-GPDs effects is in progress now [69]. It is shown that the gluon and quark sea GPDs lead to a cross section that does not decrease with energy. Thus, this reaction can be studied at high energies. We estimate the cross section at NICA energies $\sqrt{s} = 24$ GeV and $Q^2 = 5$ (GeV/c)^2 integrated over s_1 and s_2. Preliminary results for $d\sigma/(dQ^2 dt_1 dt_2)$ -in pb/(GeV/c^6 are shown in Fig.10 as a function of momentum transfers t_1 and t_2. The cross section of exclusive Drell-Yan process is equal to zero at $t_1 = 0$, $t_2 = 0$. It has a strong maximum at rather small momentum transfer and decrease exponentially at higher t_1 and t_2. At the maximum the cross section is of about $40-50$ pb/(GeV/c)^6. The integrated over t_1 and t_2 Drell-Yan cross section $d\sigma/dQ^2$ equals to ~ 3 pb/(GeV/c)^2. This value is rather small with respect to the cross section of the inclusive Drell-Yan production because the contribution, depicted in Figure 9(b), is part of an inclusive process. Estimations show that such contribution is rather small but might be visible at NICA. The J/ψ mesons can be produced in a similar way.

The light ρ, ω vector mesons production can test $H, \tilde{H}, E$ GPDs contributions. J/ψ production will give information about the gluon GPDs H^g, $\tilde{H}^g$. Exclusive Drell-Yan process with double GPDs contribution is an important test of the GPD model. Drell-Yan cross section is rather small, but hopefully attainable.

Thus, important information on GPDs structure can be obtained at NICA with polarized beams.

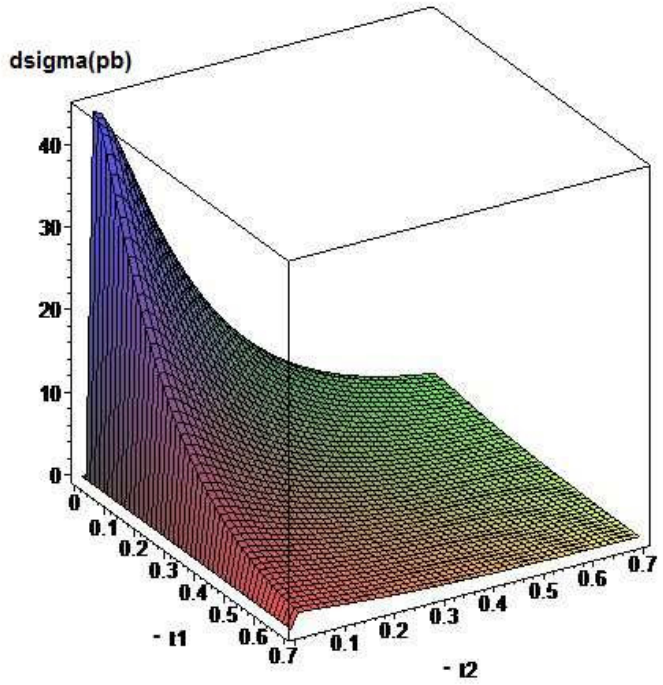

Figure 10: Preliminary theoretical results for the cross section of an exclusive Drell-Yan process over t_1 and t_2 at NICA energies and $Q^2 = 5$ (GeV/c)^2.

3 Polarized beams

3.1 Available species and types of collisions

Basic requirements for the polarization states and their combinations are fromulated below:

- proton beams: vector polarization, longitudinal and transverse direction with respect to the particle velocity;
- deuteron beams (possibly helium-3 ions at the second stage): vector and tensor polarization, vertical direction of polarization, changing of the polarization direction by 90° up to about 4 GeV/c momentum;
- possibility to collide protons with deuterons, proton with helium-3 and deuterons with helium-3 with luminosity of the order of 10^{30} cm^{-2} s^{-1} and beam momenta as in the proton-proton collisions;
- possibility of asymmetric (in momentum) collisions should be considered as an option for the future development of the facility;
- for efficient reduction of the systematic uncertainties it is desirable to have an option for rotation of the single bunch polarization direction by 90° within one turn;

Technical realization of the above mentioned conditions is feasible.

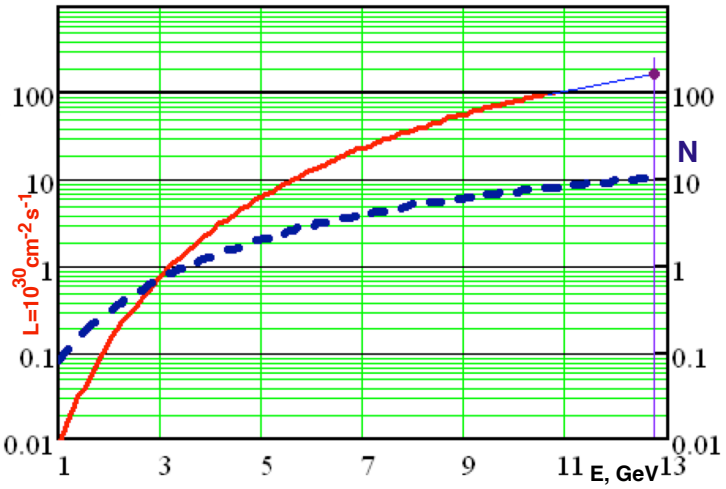

Figure 11: Normalized dependence of the pp-collision luminosity L and the beam intensity N on the proton kinetic energy.

3.2 Beam structure, intensity and luminosity

Beam structure of polarized proton and deuteron beams at the first stage will correspond to that optimized for the NICA heavy ion regime. Some of the important parameters are as follows: number of bunches = 22, bunch length $\sigma = 60$ cm, orbit length = 503 m, bunch velocity $v \approx c = 3 \times 10^8$ m/s, revolution time $\tau = 1.67 \times 10^{-6}$ s, revolution frequency of a given bunch = $f \approx 0.6$ MHz, time gap between bunches $\Delta\tau = 76.0 \times 10^{-9}$ s. The calculated dependence of the pp-collision luminosity on the energy and number of protons in the bunch is presented in Fig. 11.

As it is seen, luminosity of 1×10^{30} cm^{-2}s^{-1} is reached at bunch intensity of 10^{11} polarized protons, whereas to obtain 1×10^{32} cm^{-2}s^{-1} a multi-bunch storage mode should be used.

3.3 Polarization degree, control and monitoring

The polarization control system should deliver the following:

- both longitudinal and transverse polarization in the SPD and MPD detectors with polarization degree not less 70% and lifetime not less than the beam lifetime;
- scan over the colliding energy with a step of 0.3 – 1.0 GeV;
- operation in asymmetric with respect to the particle momentum mode;
- possibility to flip the spin of any bunch.

4 Detector setup

4.1 General design

Elaboration of a design concept for a detector capable to exploit the broad spin physics potential of the high luminosity NICA collider is one of the main tasks of the project. The proposed detector design should meet a set of requirements that corresponds to the main physics tasks described in Chapter 1 and in the Letter of Intent [21]:

- Close to 4π geometrical acceptance;
- High-precision ($\sim 50\ \mu m$) and fast vertex detector;
- High-precision ($\sim 100\ \mu m$) and fast tracking system,
- Good particle ID capabilities;
- Efficient muon range system,
- Good electromagnetic calorimeter,
- Low material budget over the track paths,
- Trigger and DAQ system able to cope with event rates at luminosity of $10^{32}\ cm^2\ s^{-1}$,
- Modularity and easy access to the detector elements, that makes possible further reconfiguration and upgrade of the facility.

A concept matching these requirements is shown in Figure 12. The SPD length along the beam axis is 920 cm, the diameter is 3.4 m and it consists of 3 parts: 2 end-caps and a barrel part. Each part has an individual magnet system: the end-caps - solenoidal coils, the barrel - toroidal magnetic system. The main detector systems, as shown in Figure 12, are as follows: Range System (for muon identification), Electromagnetic Calorimeter, Time-Of-Flight system, main Tracker and Vertex Detector (see also Figure 13). The estimated total weight of the facility is of about 1800 tonn. Such a design gives a possibility for upgrade and modification of each of the main detector systems and for performing measurements in different detector configurations. For example, for some of the physics tasks, listed in Chapter 1, e.g. detection of prompt photons, one could remove the toroidal magnet and the barrel tracker, thus decreasing significantly the material budget between the interaction point and the Electromagnetic Calorimeter.

Drawings of the endcaps and of the barrel part are given in Figure 14.

Detailed design of the mechanical support of the detector is under preparation.

4.2 Magnetic system

The basic requirements for the SPD Magnetic System (MS) are the following:

- universality, i.e. the field generating elements should be reconfigureable so the magnetic pattern of the set-up could be changed according to the needs of the physics tasks;
- minimal influence on the beam particles spin, i.e. the magnetic field should be close to zero (or minimized) along the beam axis inside the SPD;
- minimization of the material inside the detector;
- field integral of $(1 \div 2)$ T·m along the particle tracks should be provided;

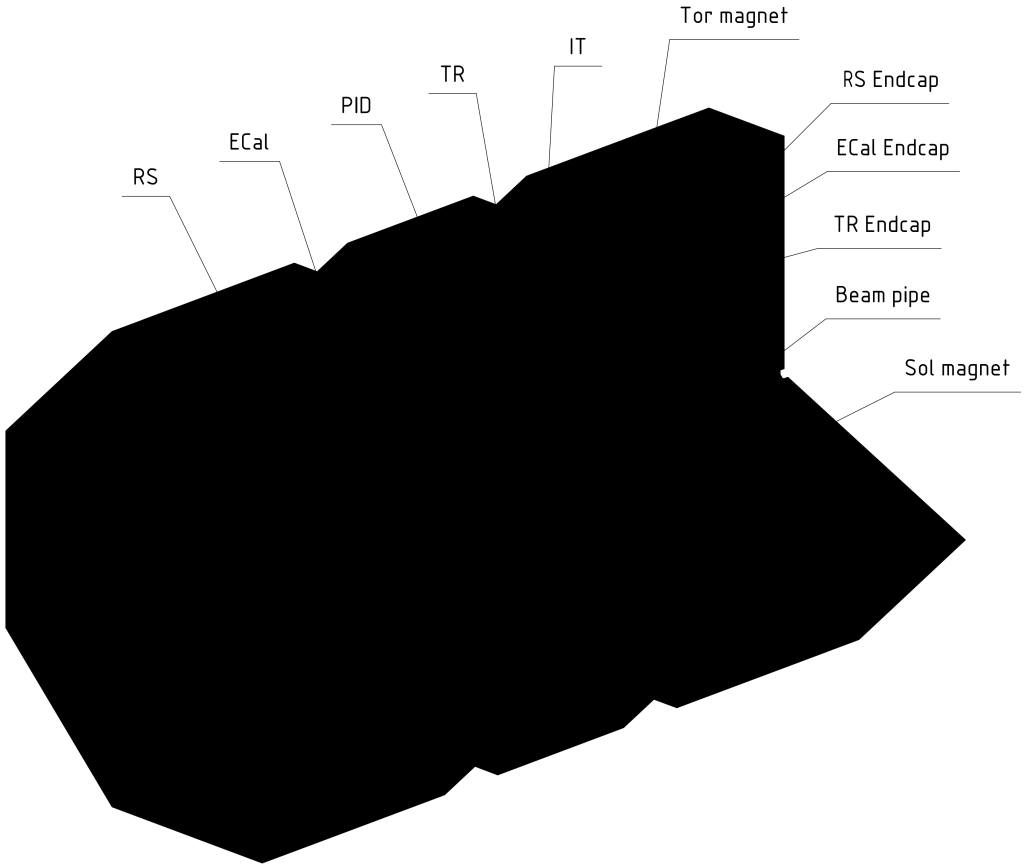

Figure 12: General view of the SPD facility.

– minimization of the total weight and coil transverse dimensions.

Different options have been considered for the MS and, at the end, a superconducting (SC) hybrid system was chosen. It consists of eight coils in the Barrel section that generate a toroidal magnetic field in the central part of the detector and two pairs of two coils each in the end-caps that produce solenoidal-type magnetic field there (see Fig. 15).

We consider two technologies for manifacturing of the SC coils: hollow high current superconducting cable similar to that used in the Nuclotron magnets (the so called Dubna type of SC cable) and a design similar to the one exploitred in the Tokamak systems, Figure 16.

A coil containing of forty turns will provide 400 kA·turns and generate the necessary magnetic field in the Barrel and in the Endcaps. With a cable diameter of 9 mm and two-layer winding one gets coil cross section of 20x180 mm^2. Of course, additional shields, insultating layers and an enveloping outer cover will be needed, see Figure 16.

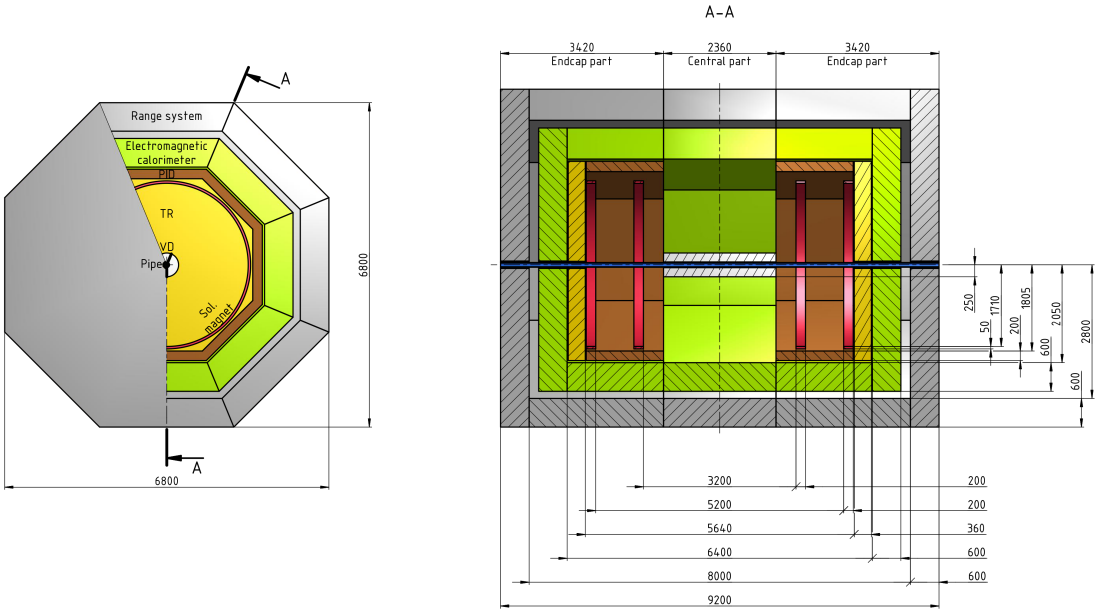

Figure 13: General dimensions of the detector.

4.3 Vertex detector (inner tracker)

The Vertex Detector (VD) is the innermost subdetector of the set-up, closely encompassing the beam pipe. Sometimes we call it Inner tracker (IT). We propose to build the VD on the basis of silicon double side strip detectors (DSSD) in combination with monolithic active pixel sensors (MAPS).

4.3.1 Overview

The VD consists of Barrel section and two Endcaps. The Barrel part is made of five layers of DSSD and three internal layers made of MAPS. The Endcaps consists of five disks of DSSD and three inner disks of MAPS (Fig. 17(a)).

The Barrel IT occupies radii between 150 mm and 550 mm (Fig. 17(b)). All five outer cylindrical layers are made of rectangular two-coordinate strip detectors and give three coordinate (r-ϕ-z) hits. The three inner MAPS layers measure all three coordinates (r-ϕ-z) of the passing tracks, too.

Registration and reconstruction of the tracks in the Endcaps takes place in the same radial region. Each of the five outer disks is made of DSSD with concentric (r) and radial (ϕ) strips.

The VD is of about 1.5 m in length and cover a pseudo-rapidity region of $\eta| < 2.5$. Each DSSD has a thickness 300 μm and a strip pitch in the range from 80 to 150 μm. The total area of the DSSD equals to 19.5m^2. The three inner MAPS layers of the Barrel and Endcaps are built from crystal CMOS pixel sensors of the ALPIDE type [ALICE Collaboration, Journal of Physics G 41 (2014) 087002] and each pixel has an area of 30x30 μm^2. The total area covered with MAPS equals to 3.5m^2.

The detector modules are mounted on very light and strong support elements with built-in cables and cooling system and form a spatial construction depicted in (Figure 18).

The VD made of 5 layers of DSSD and three inner layers of MAPS in combination with the main Straw Tubes Tracker (see Section 4.4) is the key detector system for event pattern recognition and track trajectory and momentum reconstruction.

The high granularity in ϕ and z allows to achieve coordinate resolution better 50 μm with high efficiency

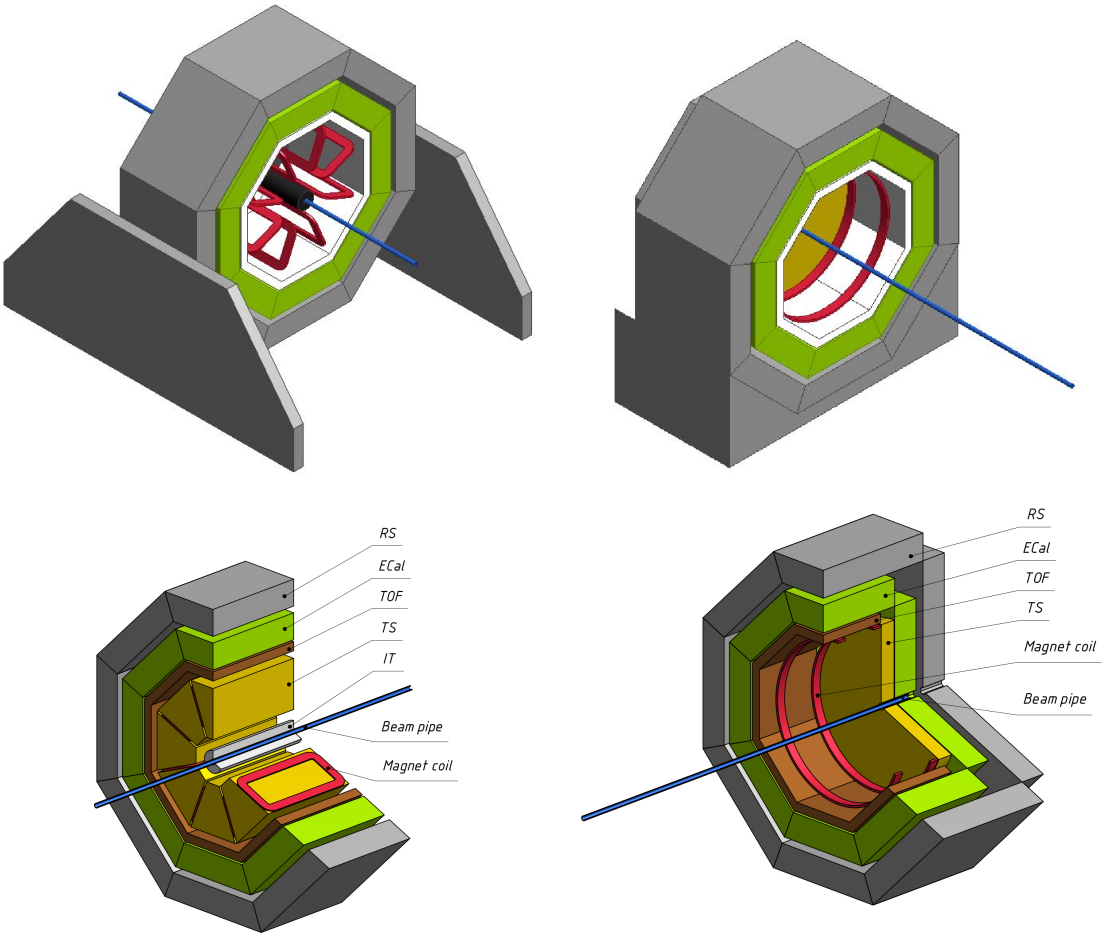

Figure 14: The Barrel section and one of the endcaps of the detector set-up.

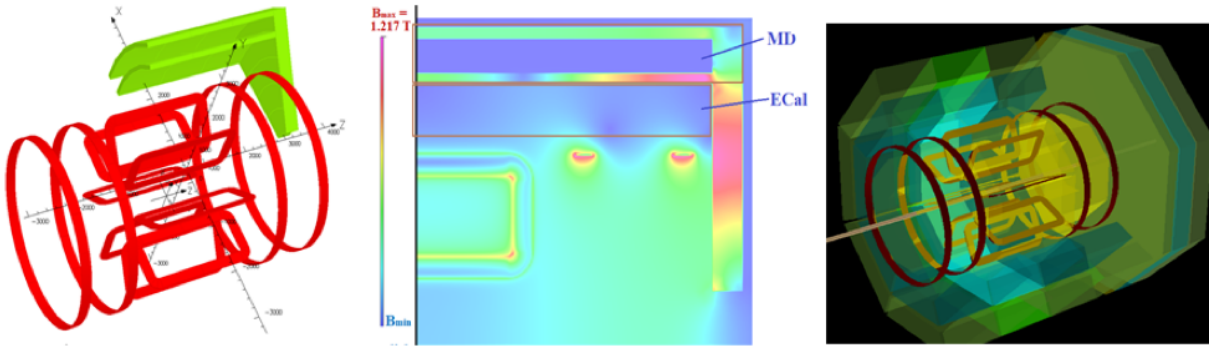

Figure 15: Hybrid magnetic system of the SPD setup.

and low single cell (strip, pixel) occupancy. The fast charge collection in the silicon detectors (less than 20 ns) will allow for separating in time of the events originating in consecutive bunch crossings. The amount of material in the tracker volume will affect the tracker performance in various ways, i.e. multiple scattering, delta electrons, photon conversion and hadron interactions. A sensor thickness of 300 μm equals only to 3.2×10^{-3} X_0. Composite materials and multilayer's aluminized capton cables and hybrids will be used to reduce the material budget of the cabling and support structures. The mechanical design and electrical circuitry of the DSSD modules could follow closely those of the silicon sensors of the BM@N experiment.

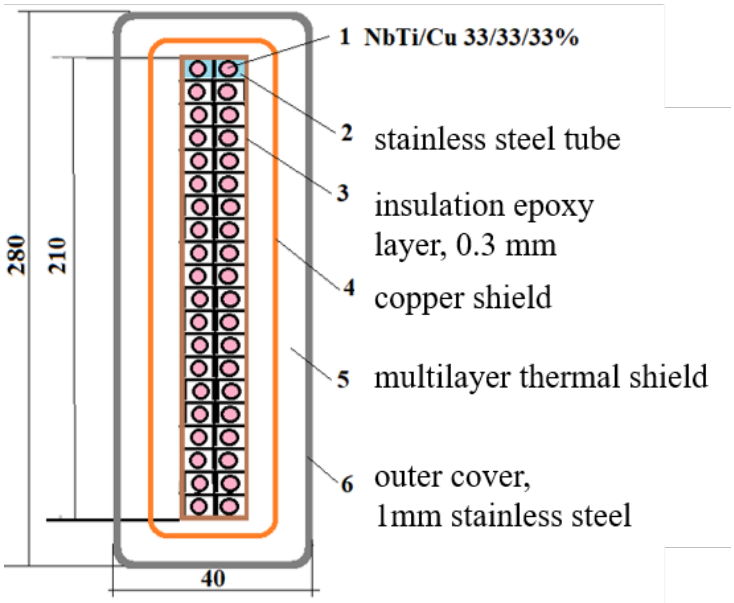

Figure 16: Cable structure of Tokamak type with 40 SC wires in a common cover.

4.4 Main tracker

The main tracker has to provide enough number of hits over the charged particle trajectories in the magnetic field and with enough precision ($\sim 100\mu m$) in order to reconstruct the charged particle tracks and event topology with good confidence.

The basic detection elements are thin-wall gas-filled drift tubes. A technology for fabricating of thin-wall (straw) drift tubes of 10 or 20 mm diameter using metalized polyethylene terephthalate film $36\mu m$ thick by ultrasonic welding is developed in the Laboratory and successfully used in other experiments (NA62).

The high strength, the low tensile creep due to the absence of glued layers, negligible gas leakage and reliability in long-term operation make these tubes an excellent candidate for the detector elements of our main tracker.

The barrel part of the Straw Tubes Tracker (STT) will consist of 8 stations situated between the eight SC magnet coils (see Figure 19).

All together, the barrel STT has a cylindrical shape with an inner radius of 500 mm, an outer radius of

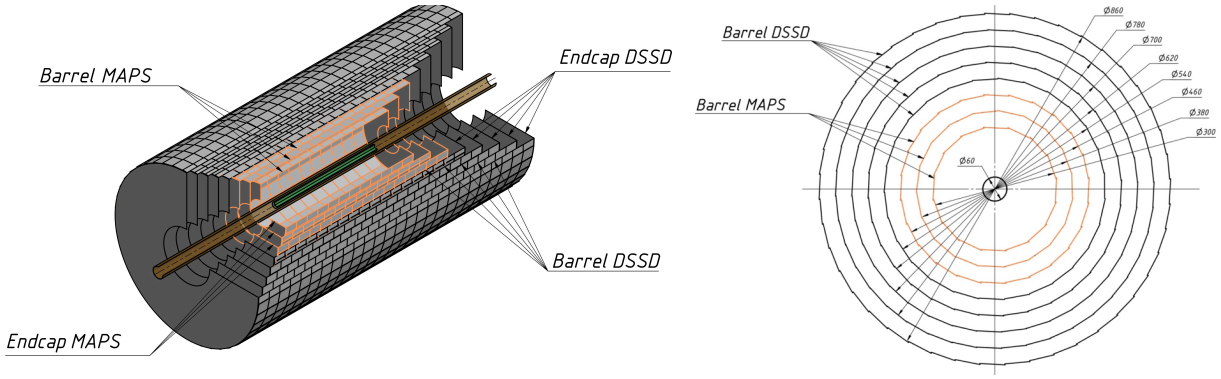

(a) (b)

Figure 17: (a) Cross section of the Vertex Detector of the SPD. (b) Five outer cylindrical DSSD layers and three inner MAPS layers of the Barrel VD.

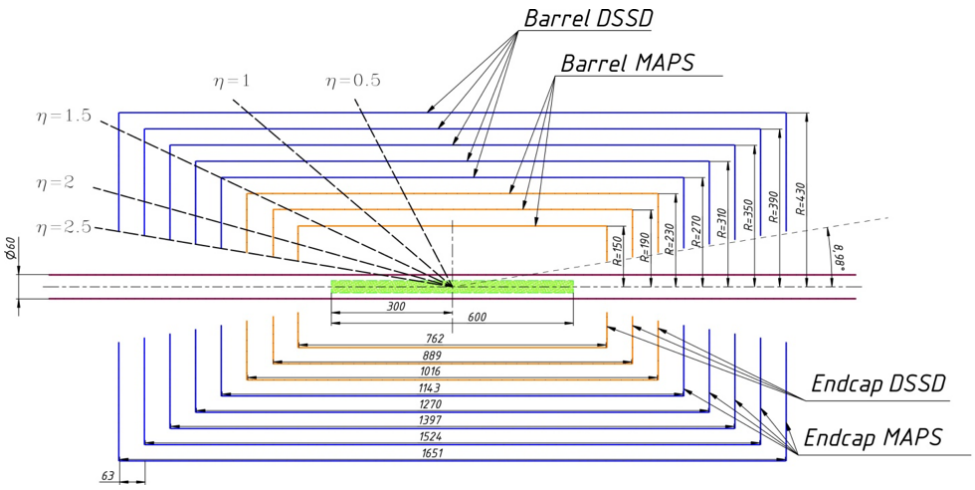

Figure 18: Cross section of all layers and disks of the VD with indicated dimensions.

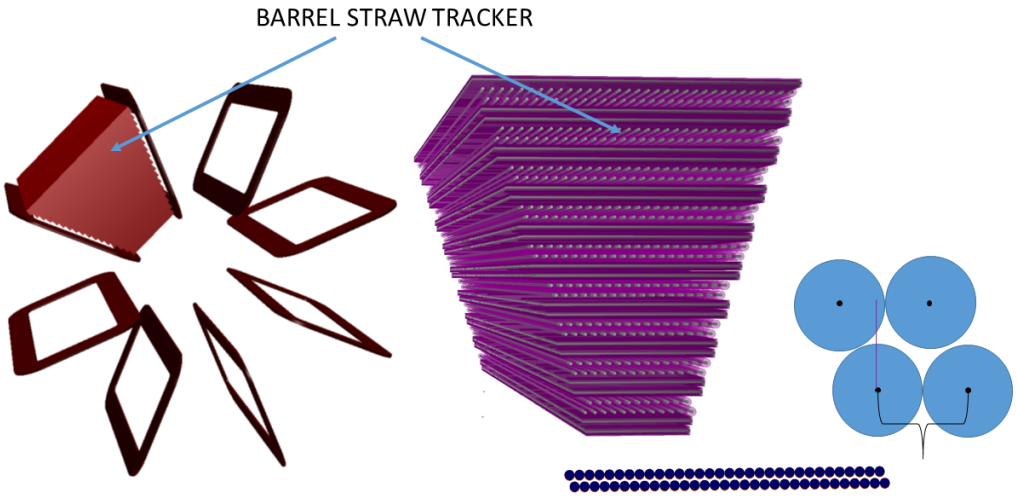

Figure 19: Sector of the Barrel straw tracker. It consists of ten double layers with tubes parallel to the toroidal magnetic field direction and other ten layers, interleaved with the formers and making a certain stereo-angle with them

.

1760 mm and length of 1960 mm. All straws have a diameter of 10 mm. Each straw tube has a 30 μm thick gold plated tungsten anode wire in the center. The gas mixture will be Argon and CO_2 as quencher. We plan to work with gas gain not greater than 10^5 in order to warrant a long term operation. Multiple layers of straws are positioned in such a way that half of them run in direction orthogonal to the beams and the other half make a certain stereo-angle with the first. This will allow for a 3D reconstruction of the trajectories of the particles. The overall design results in a material budget of 1.2% of the radiation length.

The tubes in the layers in the end-cap parts are oriented mainly in parallel to the beam with some of them forming a certain stereo-angle with the beam direction.

4.5 Electromagnetic calorimeter

The electromagnetic calorimeter (ECal) of the SPD setup is situated inside the Range System and consists of three parts: the barrel one and two end-caps. The calorimeter should meet the following requirements:

- energy range from 50 MeV to 10 GeV;
- energy resolution of about $5\%/\sqrt{E\ [GeV]}$;
- granularity ~5 cm;
- time resolution ~ 0.5 ns;
- operation in magnetic field;
- long time stability of the basic parameters $\pm 5\%$.

We propose a design based on the sampling calorimeter [70]. It is made of alternating layers of lead and scintillator plates with fine granularity. A single tower of the KOPIO calorimeter made of four independent modules is shown in Fig.20. A single module consists of 220 layers of scintillator (1.5 mm thick) and lead (0.3 mm thick) plates with transverse dimensions of 5.5×5.5 cm^2. Wave-length shifting fibers pulled inside the module collect the scintillation light to four avalanche multipixel diodes or SiPMs. The length of the active part of the module will not exceed 450 mm. Together with the readout electronics it should fit into 600 mm. A schematic layout of the SPD ECal is shown in Fig. 21.

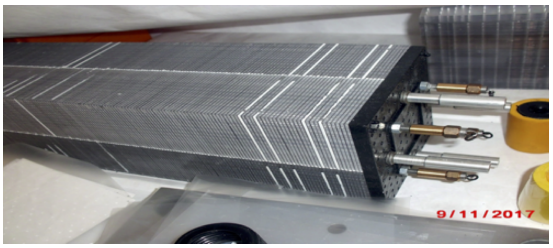

Figure 20: A tower made of 2x2 modules of the KOPIO sampling calorimeter. Each module consists of 320 lead plates 0.3 mm thick and the same number of scintillator plates of 1.5 mm thickness each.

The barrel part of the ECal is made of 3 rings (a middle and two side ones) with 8 azimuthal sectors each. The side rings consist of 2080 towers while the central one is made of 2288 towers (6448 towers in total. The end-cap parts are planned as two discs with diameter of about 3.6 m and beam hole of about 20 cm. The number of towers in each end-cap disc is 850. The expected weight of the barrel part and the end-cap parts is 81 tons and 11+11 tons, respectively. Assuming that the weight of the supporting structures would not exceed 15%, the total weight of the SPD ECal could be estimated as 118.5 tons.

The expected resolution of the proposed sampling calorimeter is

$$\sigma_E/E = (1.96 \pm 0.1)\% \oplus (2.74 \pm 0.05)\%/\sqrt{E}. \quad (4)$$

4.6 Range System

4.6.1 General description

The Range System (RS) serves for the following purposes in the SPD:

- identification of muons in presence of a rather high hadronic background;

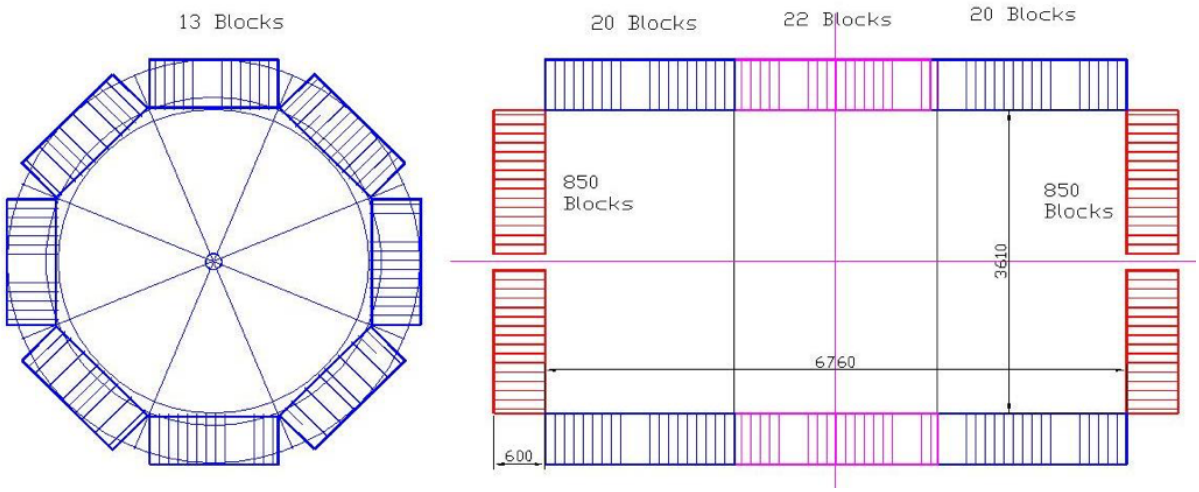

Figure 21: Schematic layout of the SPD electromagnetic calorimeter.

– rough measurement of the energy of the hadrons (coarse hadron calorimetry).

It is the only device in the SPD setup that could detect neutrons and measure their energy. The identification of muons is performed via pattern recognition and matching of the track segments in the RS to the tracks in the tracker. Mini Drift Tubes (MDT) two-coordinate readout (wires and perpendicular strips) [71, 72] are used as tracking elements in the system. In the design and construction of the present system we shall capitalize on the experience gained by the JINR group in development of the PANDA (FAIR, Darmstadt) Muon System. The latter is designed to identify muons in a similar momentum range that makes it a good prototype for the SPD one.

4.6.2 System layout

The Range System consists of a Barrel section and two Endcaps. They serve as absorber for the hadrons and 'filter' for the muons. A schematic 3D view of the system is shown in Fig.22. The Barrel is divided in three equal parts due to the type of magnetic system, and each End Cap consists of two halves. The total weight of the system is about 1268 ton (828 ton for the Barrel and 220 ton for each End Cap).

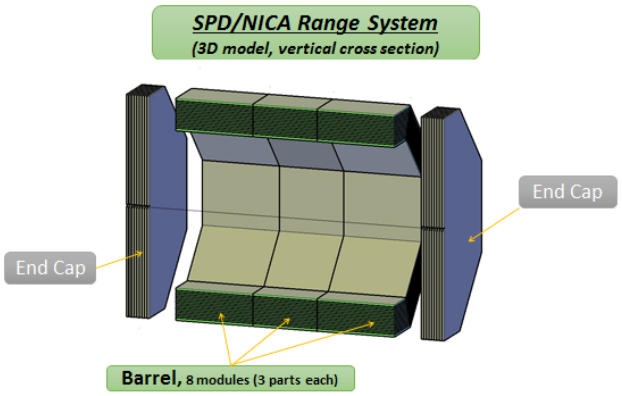

Figure 22: 3D view (half cut) of the Range (muon) system.

Due to the different momenta spectra for the central (Barrel) and forward (Endcaps) regions the sampling of the steel plates is also different: 3 cm thick Fe plates for the Barrel section and 6 cm – for the Endcaps. Figure 23 demonstrates the Barrel and End Cap structures in more detail. The outer 6 cm Fe layers are used in both cases for assembling/bolting the modules together. In the interlayer gaps of 35 mm the

MDT elements together with the strip boards and front-end electronic boards are mounted. on them. The thicknesses of the Barrel and Endcaps are almost the same - 3 and 2.8 nuclear interaction lengths (λ_I), respectively. This way an equal muon filtering at all directions is achieved. Together with the ECal ($\sim \lambda_I$) the total thickness of the SPD setup is about 4 λ_I.

(a) (b)

Figure 23: Structure/sampling of the Barrel (a) and Endcaps (b).

4.6.3 Mini drift tubes

MDTs of this type were initially developed and produced in JINR for the Muon System of the D0 experiment at FNAL [73]. Later,the same tubes were used in the COMPASS experiment at CERN [74]. After developing of two-coordinate readout by modifying the geometry and adding external pickup electrodes (strips), the new MDT design was accepted by PANDA project at FAIR. This new version of the MDT is proposed for the SPD project. because it has all the necessary features – radiation hardness, coordinate accuracy, time resolution, robustness, as well as good level of maturity due to already performed R&D within the PANDA project.

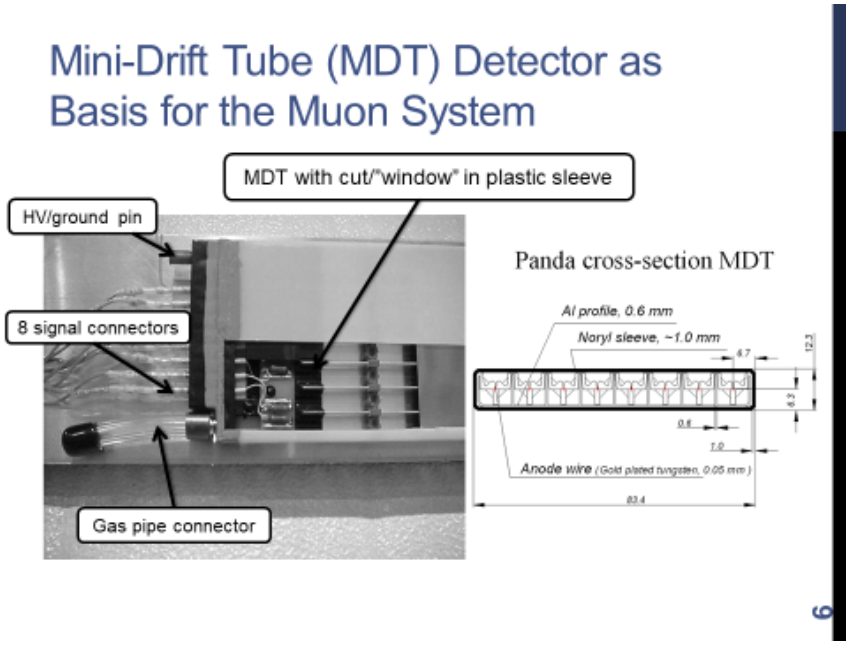

Figure 24: Layout and cross section of the MDT elements.

The layout of the MDT is shown in Fig.24.

4.6.4 *Performance*

Evaluation of the main parameters of the proposed Range System is being performed with a 10 ton prototype installed at CERN within the PANDA program.

Fig. 25 gives examples of the prototype response to different particles. The patterns demonstrate the excellent PID capabilities of the Range System.

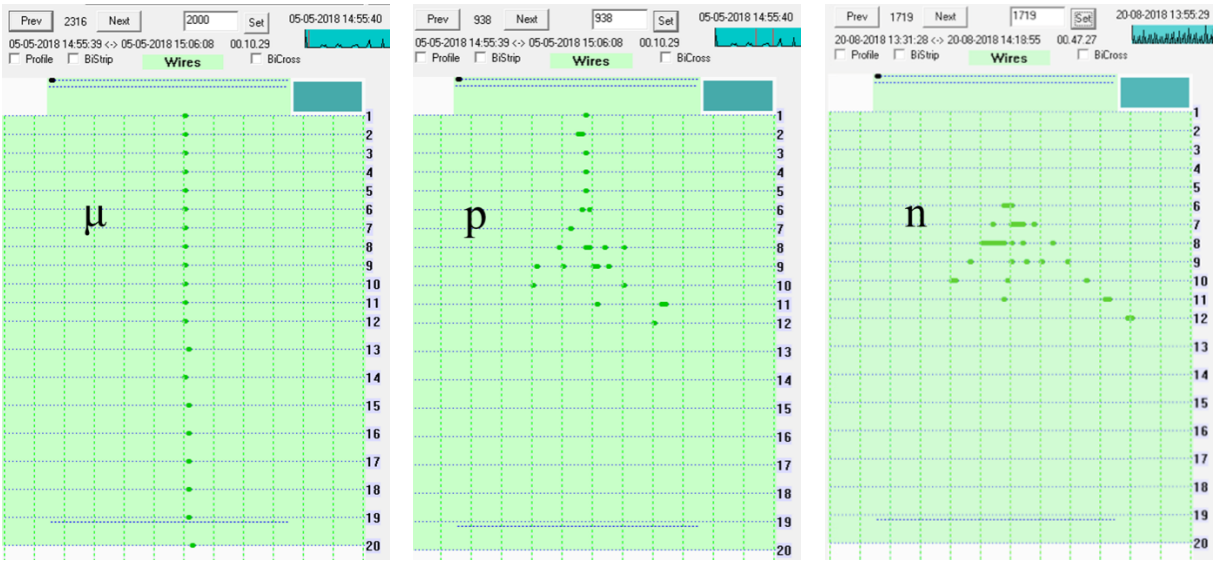

(a) (b) (c)

Figure 25: Demonstration of PID abilities: patterns for - (a) muon, (b) proton and (c) neutron.

4.7 Particle Identification System

The PID system is expected to cope with particle flux of up to 10 kHz/cm^2 and should allow:

- muon identification in the energy range 0.5 – 10 GeV;
- electron/positron – hadron separation in the same energy range;
- pion/kaon/proton separation.

The identification of muons will be performed by the Range System (see sect. 4.6). The main instrument for separation of hadrons from the electrons/positrons will be the ECal (see sect. 4.5). For π/K/p identification a dedicated system is needed. One of the options under consideration is a time-of-flight system.

4.7.1 *SPD ToF system*

Time-of-flight spectra of hadrons with different momenta over 2 m flight path are given in Figure 26.

As it is seen, a ToF system with combined start-stop time resolution of $\approx$ 30 ps could separate pions from protons up to $\approx$ 5 GeV/c. For larger momenta different techniques should be used.

A possible ToF detector for SPD could be multi-gap resistive plate chamber (mRPC) with electrodes made of low-resistivity thin glass (less than $10^{10} - 10^{11}$ $\Omega\cdot$ cm) [75–78] or ceramics [79]. For instance, time resolutions below 90 ps and efficiencies larger than 90% were obtained for particle fluxes up to 25 kHz/cm^2 for the 10-gap mRPC [77]. Further decrease of the glass stack resistance could be achieved by decreasing the electrode thickness and increasing of the temperature of the glass. It was shown that such

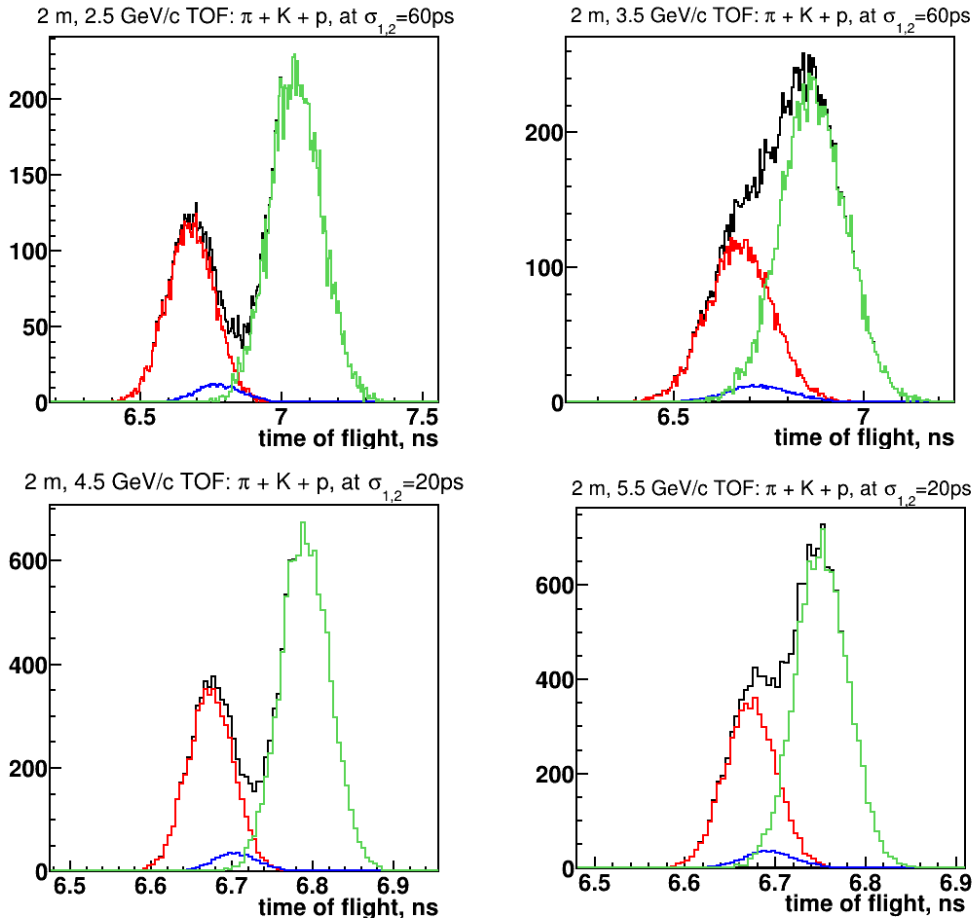

Figure 26: Time-of-flight spectra of hadrons with indicated momenta and for two values of the time resolution $\sigma_{1,2}$ of the start and stop detectors.

a method can provide high time resolution at rates up to 20 kHz/cm^2 [80]. There is an on-going R&D in the Laboratory of High Energy Physics for design of high-speed glass mRPC with time resolution below 50 ps.

4.8 T0 counter

The T0 counter design follows the early ALICE collaboration concept [**?**] based on an array of multi-anode micro channel plate (MCP) [82**?**] detectors with isochronous read-out of their signals. The readout uses "noise-free" isochronous summation of the MCP signals by a passive summator (see Fig. 27).

The majority of the secondary particles emerging from any relativistic collision reach the T0 detector plane almost simultaneously (within 100 ps). Thus, the isochronous readout provides one analog signal after summation of the signals from the anodes of the MPCs. This 1 ns wide analog signal, coming from the detector plane, contains timing and multiplicity information for the event. Two different detector designs are considered: each detector (Figure 28(b)) is situated in its own vacuum chamber (as in Figure 28(a)), or the whole detector plane is mounted inside a singe vacuum chamber around the beam chamber.

The proposed detector provides adequate (about 30 ps) time resolution of the start (T0) signal (leading edge rise time less than 1 ns). It is proposed as a part of the beam-beam counters system for providing of the T0 signal. It also could help in monitoring of the beam polarization.

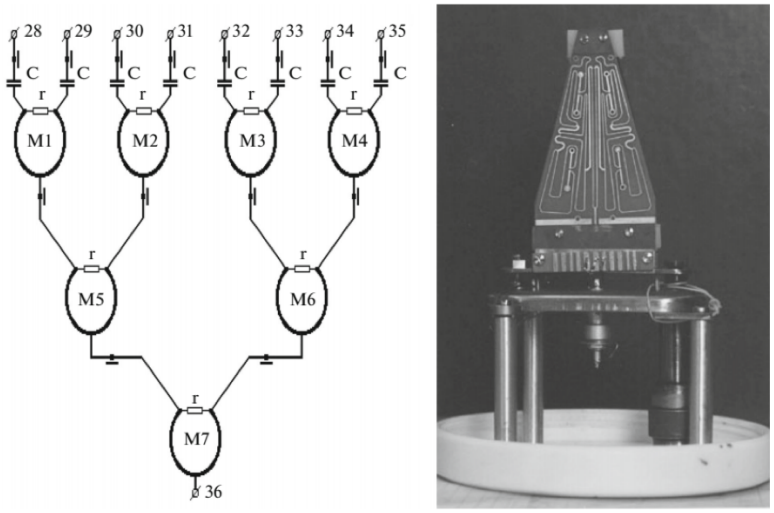

Figure 27: Electrical scheme of the isochronous passive summation based on application of circular bridges of short (1 ns FWHM) signals coming from the anodes (pads) of the MCP detectors (left) and its realization in microstrip technology (right) [81**?**].

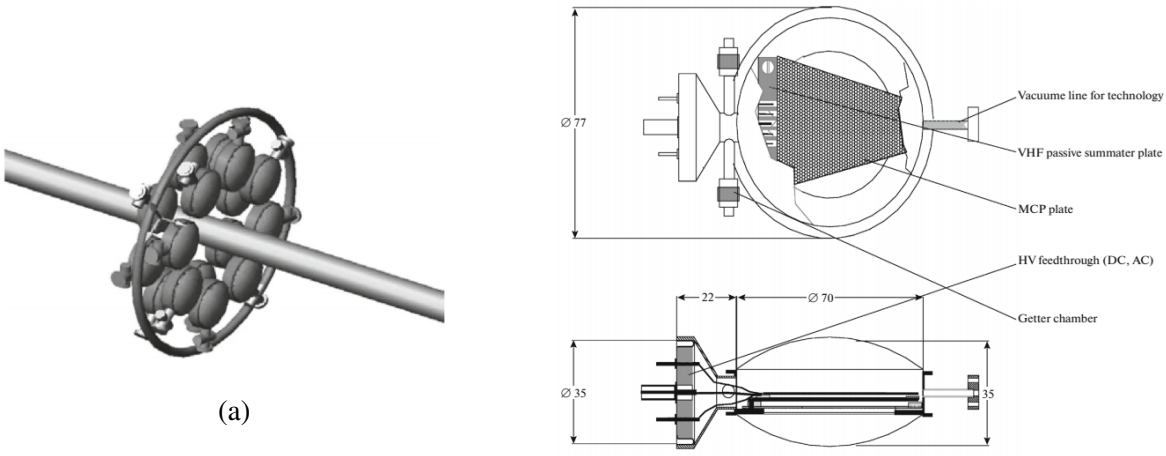

(a)

(b)

Figure 28: (a) Conceptual design of timing and multiplicity detector consisting of 16 MCP detectors each of them placed inside a separate vacuum chamber around the beam line. (b) General design of the MCP detector embedded into a thin-wall (200 μm) Ti lens-type vacuum chamber [81**?**].

4.9 System for local polarimetry

The system for local polarimetry of the SPD should perform monitoring of the beam polarization during data taking with an aim to reduce systematic uncertainties coming from the beam polarization variation.

We are going to perform measurements in an unexplored energy range below $\sqrt{s}$=27 GeV, where polarization data are scarce thus making difficult finding of suitable reactions for polarization measurement. We consider several processes discussed in turn below.

4.9.1 Asymmetry in inclusive production of charged particles

One of the tools to control the proton beam polarization is measurements of the azimuthal asymmetry in inclusive production of charged particles in collision of transverse polarized proton beams. Such a method is used at the STAR detector. Two Beam – Beam Counters (BBCs) consisting of suitably

assembled hexagonal scintillation tiles of two different sizes are used for this purpose. BBCs detect charged particles produced under small angles in both forward directions.

Signals from the counters are used for three different purposes. The first one is to indicate whether the beam-beam interaction has taken place and to suppress the beam-gas interaction. The second task is to estimate the beam luminosity and to provide T_0 signal for the trigger and ToF systems. The third task is to monitor the transverse beam polarization and spin rotator settings by measuring the azimuthal asymmetry of the counts.

The value of the effective analyzing power A_N for inclusive production of charged particles at $\sqrt{s}$= 200 GeV is about $6 \div 7 \times 10^{-3}$. At NICA energies it should have, in principle, the same or even larger value due to the larger analyzing power of the pp- elastic scattering at lower energies. Therefore, similar BBCs could be used for performing of local polarimetry at the SPD.

4.9.2 Single transverse spin asymmetry for very forward neutron production

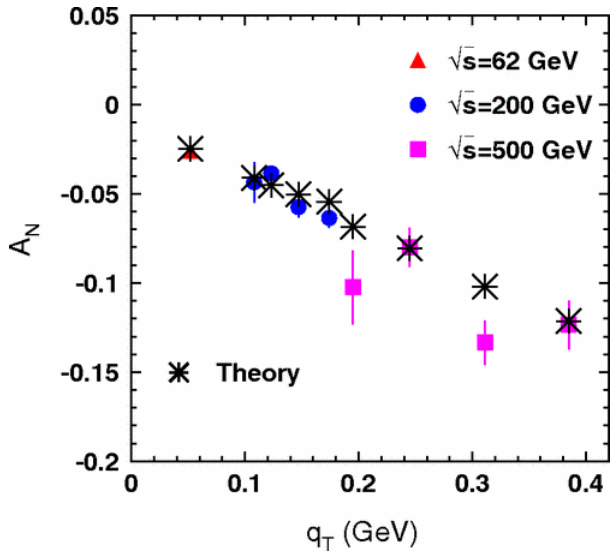

Figure 29: Single transverse spin asymmetry A_N in the reaction $pp \to nX$, measured by PHENIX detector at $\sqrt{s}$= 62, 200, 500 GeV. By asterisks results of the theoretical calculations [83] are shown.

The energy dependence of the single transverse spin asymmetry, A_N, for neutron production at very forward angles was measured by PHENIX experiment at RHIC for polarized p+p collisions at $\sqrt{s}$=200 GeV [84]. The neutrons were detected in forward detectors covering an angular range of up to 2.2 mrad. The observed forward neutron asymmetries were large, reaching A_N=-0.08±0.02 for x_F=0.8; the measured backward asymmetries, for negative x_F, were consistent with zero.

The observed large asymmetry for forward neutron production was discussed in the pion exchange framework by a model based on an interference between the pion exchange spin-flip amplitude and non-flip amplitudes of all other Reggeon exchanges. The numerical results of the parameter-free calculation of A_N are in excellent agreement with the PHENIX data (see Fig.29. One can see that A_N is increasing almost linearly as a function of q_T. One can expect the A_N value of ∼-0.02 at $\sqrt{s}$=27 GeV. Therefore, the $pp \to nX$ reaction with neutron emission at very forward angles can be used at SPD for local polarimetry.

4.9.3 Inclusive $pp \to \pi^0 X$ reaction

One of the reactions to measure and monitor the vertical polarization of the proton beam is the inclusive $pp \to \pi^{\pm,0} X$ reaction. Fig.30 demonstrates the single transverse spin asymmetry A_N obtained in proton-proton collision for π^+, π° and π^- inclusive production at 200 GeV ($\sqrt{s}$ ∼20 GeV)[85, 86]. The data

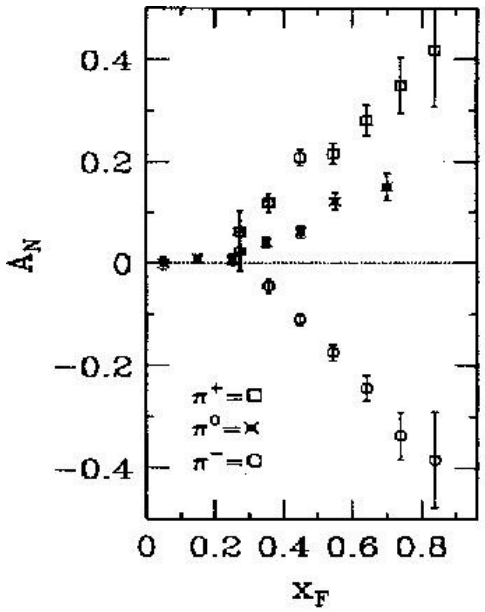

Figure 30: Single transverse spin asymmetry A_N for inclusive pion production in pp- collisions at 200 GeV [85, 86].

demonstrate its large value and with sign following the polarization of the valence quarks in the pions. Such a regime happens already at 22 GeV [87] corresponding to $\sqrt{s_{NN}} \sim 7$ GeV. Therefore, inclusive pion production can be used for polarimetry over the full energy range of the SPD experiment.

The value of the single transverse spin asymmetry in $pp \to \pi^0 X$ reaction is about twice smaller than for the charged pions production. However, the π^0 selection can be done easier since it does not require track reconstruction. For the purpose of the local polarimetry one can use several towers of the electromagnetic calorimeter placed around the beam pipe or a special calorimeter with a suitable design. In both cases development of fast algorithms for the π^0 selection in this very forward calorimeter is required.

4.10 Data acquisition system and slow control

The data acquisition system of the SPD should provide:

- continuous data taking, including data readout from the front-end electronics, data consistency check, event building and writing events to a storage;
- minimal dead-time or dead-time-less DAQ operation.

Other important tasks of the DAQ are:

- control and monitoring of the data taking process: control of the status of all hardware devices, status of software, quality of collected data;
- monitoring of the parameters characterizing the detector performance (accumulation of time, amplitude and hit distribution histograms, detector rates);
- slow control of the detector settings;
- logging of information and errors;
- distribution of the data over the computing nodes for on-line analysis;

To build the data acquisition system of SPD, it is planned to use as a basis the recently modernized DAQ of the COMPASS experiment [88, 89]. This intelligent DAQ uses contemporary Field Programmable Gate Array (FPGA) technology. It allows to work with large data streams with minimal latency and provides very good flexibility.

The critical parameter of any DAQ is its rate capability. The present configuration of the COMPASS DAQ provides a bandwidth of 500 MB/s sustained rate. By buffering and exploiting the spill structure of the SPS beam, the maximum on-spill data rate reaches 1.5 GB/s and the DAQ can handle peak data rate of 8 GB/s. In [88] it was stated that using the FPGA of the most recent generation, one could attain in COMPASS a data throughput up to 10 GB/s and, with a moderate investments, even up to 100 GB/s.

In the NICA collider, there will be no spill structure and the SPD DAQ should withstand high data rate of a continuous beam. Modification of the spill-structured algorithms of the COMPASS DAQ to conditions of the continuous operation of the SPD DAQ may become one of the main challenges.

Some preliminary rough estimations of the data flow in the SPD are given below. At the maximum energy $\sqrt{S} = 26\ GeV$ and the maximum luminosity $L = 10^{32} cm^{-2} c^{-1}$, the expected event rate within the SPD aperture is $3 \cdot 10^6\ s^{-1}$. A total number of the detector channels in SPD is about 500 000, with the major part coming from the vertex silicon detector. Assuming that all sub-detectors are in operation (vertex detector, straw tracker, mRPC based ToF detector, electromagnetic calorimeter, range system), the raw data flow is estimated as 10–20 GB/s.

Two modes of the DAQ operation are under consideration: trigger-controlled and trigger-less ones. The choice between the trigger-controlled and trigger-less modes will be done after refining the expected data flows. The trigger-less mode may be used if the DAQ is capable to read out all the data without trigger selection. In this mode readout of all the detectors is carried out in time slices with a fixed frequency, with subsequent data reduction by means of on-line algorithms implemented in FPGA chips and computers.

The expected structure of the SPD DAQ is as follows (Fig. 31). The data from the front-end electronic channels come to data concentrator modules. If the trigger signal (or readout frequency clock signal in a trigger-less mode) arrives, the readout is performed. To create subevent, a time-stamp and event identifier are added. Next, the event builder performs on-line data consistency check and applies programmable error recovery algorithm. The event builder is arranged in two layers of FPGA cards. FPGAs of the first layer are configured as multiplexers receiving data from the data concentration modules via optical links. Second layer FPGA is programmed as a switch and distributes fully assembled events to readout computers. The events are temporarily stored in a local storage and finally are recorded in a permanent data storage.

In the case of trigger-controlled DAQ, the trigger system may include two levels: local triggers L0 produced by the sub-detectors (ECal, RPC-ToF and Range System are the candidates for L0 generation), followed by the central trigger processor which analyses all L0 signals and produces the final trigger decision. Front-end electronics for this mode should have a sufficient depth of the queue to cover the possible trigger latency.

Independent from a real-time data readout process but very important task of the DAQ is the slow control. The slow control software communicates with interfaces of the devices that measure the values of many slowly changing parameters: high and low voltages, magnetic field, temperature, gas flow, etc. The implemented alarm system issues a warning when any of the parameters gets out of the tolerance limits. Another task, which can be attributed to the slow control, is configuration and remote control of the hardware.

The current project includes as a component creation of a SPD test zone at one of the extracted beams of the Nuclotron. The DAQ for the test zone will be different from the main one, it will be close to the traditional DAQ systems based on readout blocks put in VME crates. Based on the requirements of the

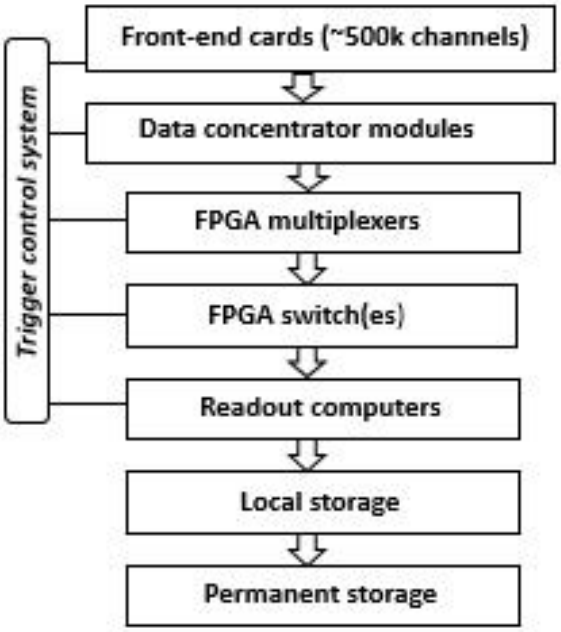

Figure 31: Structure of the SPD DAQ.

given test the DAQ configuration will be adapted accordingly. At a later stage, when combined tests of the detectors are performed in the test zone, the components of the main DAQ will be used there, and this will be the test of the main DAQ itself.

5 Beam test facility

For beam tests of the anticipated prototypes of the SPD detectors and systems in beams of pions, kaons, protons, neutrons, muons, electrons, and light nuclear fragments it is proposed to create a test beam zone in one of the extracted beams of the Nuclotron. The test zone will include the refurbished and modernized magnetic spectrometer MARUSYA (momentum range 0.4–1.2 GeV/c) and a newly formed high momentum channel (HMC) where beams with 1–10 GeV/c momenta will be available. Both test beam channels will provide tracking and PID per particle.

Figure 32 shows the drawing of the considered magnetic elements in both channels.

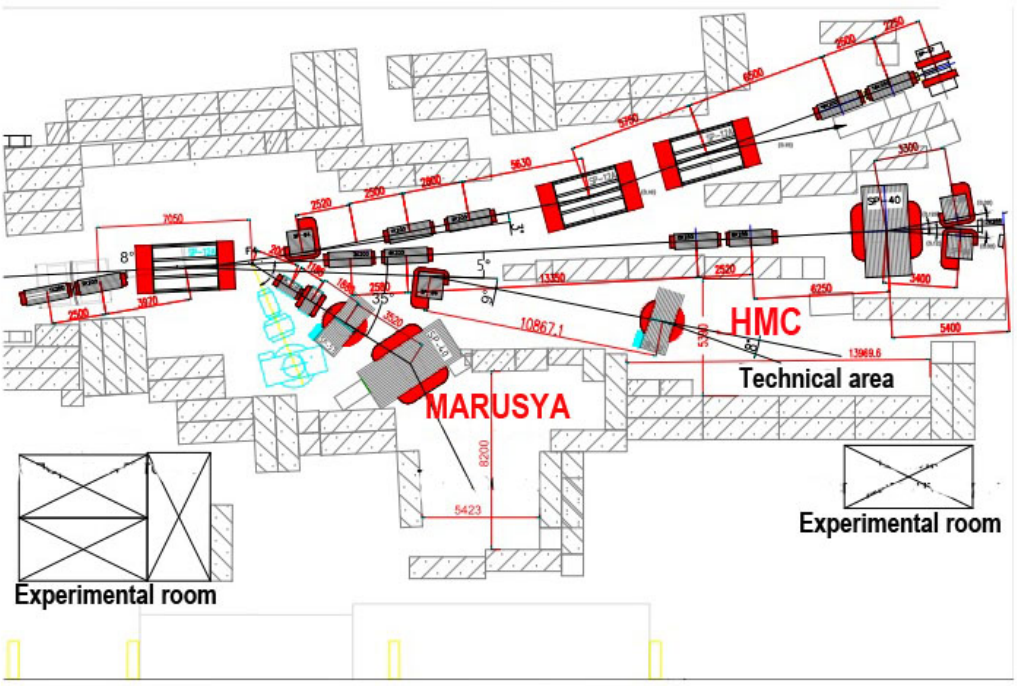

Figure 32: Magnetic elements of the low momentum (0.4–1.2 GeV/c) test beam channel MARUSYA and of the high-momentum (1–10 GeV/c) Channel HMC.

Both simulations and measurements in deuteron, carbon, magnesium, lithium, etc. beams showed that the spectrometer MARUSYA provided the following parameters: for an extracted 2-4 GeV/n deuteron beam with an intensity of 10^10 and carbon and copper targets with a thickness of 1 g/cm^2 secondary pion beams with an intensity of 10^4 can be obtained. The size of the the last magnet (SP40) is $100 \times 150 mm^2$. A scintillator based ToF system has demonstrated reliable identification of protons, pions and kaons in the momentum range 600–1200 MeV/c.

With 5 GeV/n deuteron extracted beam and a carbon target with a thickness from 0.005 to 5 g/cm^2, the attainable beam parameters in MARUSYA are given in rows 1–3 of Table 1, and in the high-momentum channel - in rows 4–5 of the same table.

The construction of the SPD test zone consists of the following stages:

- Cleaning of the zone, removal of unnecessary elements (magnets, lenses, detectors, etc.). Refurbishment of the shielding blocks and walls;
- Renovation and repair of the experimental rooms, installation of new electrical supply lines, etc.

Table 1: Attainable total particle fluxes per spill in MARUSYA test channel (rows 1–3) and in the high-momentum channel HMC (rows 4–5).

P, MeV/c	d	p,n	$\pi^{\pm}$	K^{+}	K^{-}	$\mu^{\pm}$	$e^{\pm}$
400	10^3	10^5	10^5	10^3	10^2	10^3	10^3
800	10^3	10^4	10^4	10^3	10^2	10^3	10^3
1500	10^2	10^4	10^4	10^3	10^2	10^2	10^2
2000	10^4	10^5	10^4	10^3	10^2	10^2	10^2
7000	10^4	10^6	10^3	10^3	10^2	10^2	10^2

Reconstruction of electrical control units for powering of the detectors and auxiliary equipment;

– Installation of a gas system;

– Upgrade of the existing and manufacturing of new beam-line detectors for tracking and PID, and also of the electronic elements of the DAQ and slow control systems;

– Acquire relevant computer equipment for the data acquisition, communication, and slow control systems.

– Mounting of two magnets in the (new) high momentum channel. Geodesic and magnetic field measurements.

6 Integration and Services.

The SPD facility is foreseen to be allocated in the south beam interaction point[90] as shown in Figure 33.

Figure 33: Layout of the NICA collider with SPD at the south collision point..

The design of the SPD hall follows closely the one of the MPD[91].

The SPD hall, as shown in Figure 34, consists of Assembling area and Experimental pavilion. The Assembling area will be used for assembling and testing of the detector systems and for maintenance works.

The dimensions of the SPD hall are given in Figure 34. The surface area is more than 2000 m^2, the main gate for trucks is 4 m x 4 m. In addition, there is a dis-mountable part of the wall with dimensions 8 m x 8 m for bringing in of very large equipment.

6.1 Service systems

The SPD sub-detectors will need a set of service systems, main of them listed below:

- Magnet: Power supply, cryogenic system
- Vertex Detector: HV power supply system, LV power supplies for powering of digital and analog electronics, cooling system for maintaining of stable work temperature;
- Starw Tubes Tracker: HV power supply system, LV power supply system, Gas mixing system;
- ToF system: HV power supply system, LV power supply system,gas mixing system;
- ECal: HV power supply system, LV power supply system, cooling and thermo-stabilization;
- Range system: HV power supply system, LV power supply system, Gas mixing system;
- Tagging station:HV, LV;
- Local polarimetry: HV, LV, cooling.

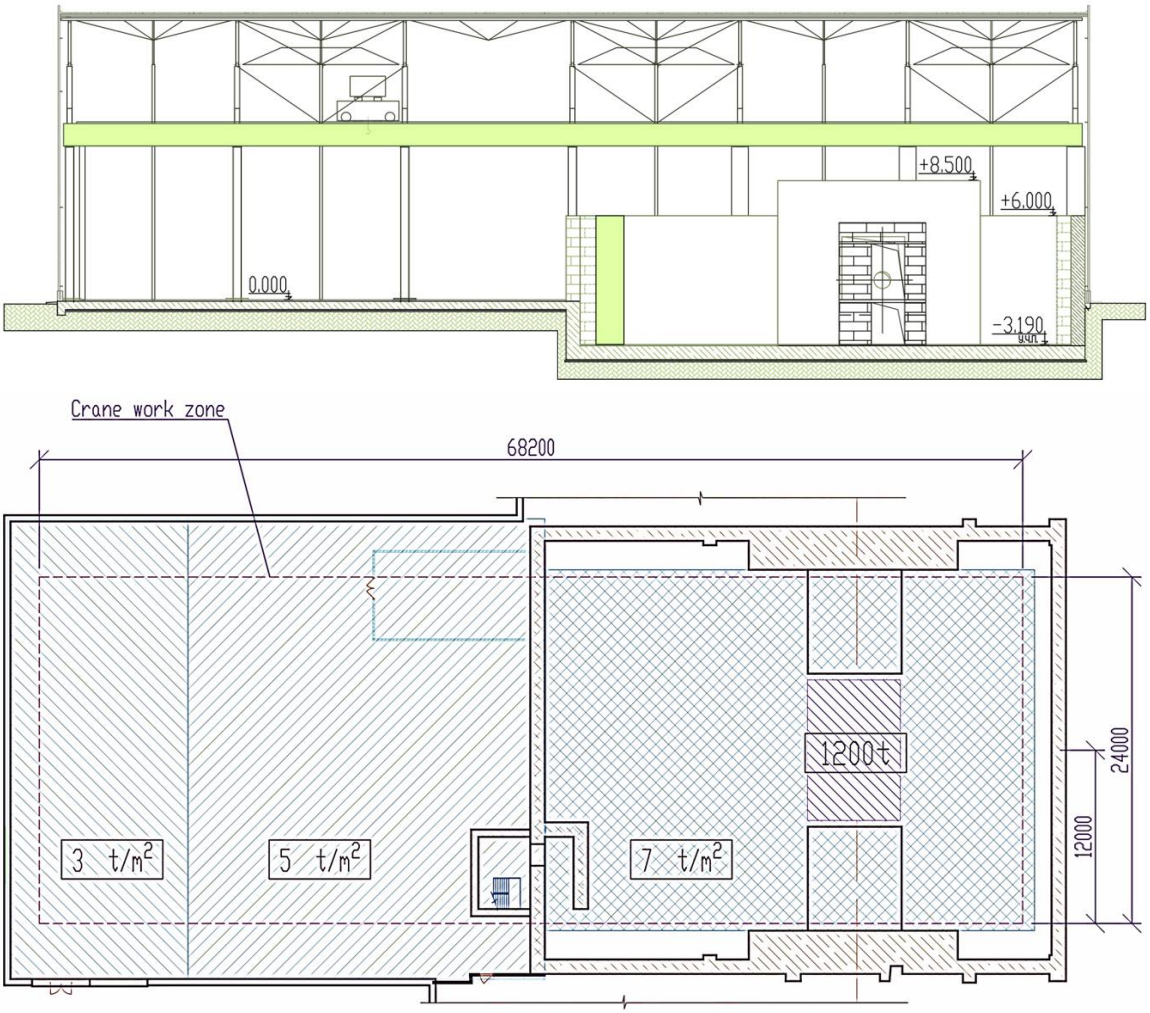

Figure 34: The SPD experimental hall.

7 Software design and computing

7.1 SPDroot

Monte Carlo simulation, event reconstruction for both simulated and real data, data analysis and visualization are planned to be performed by an object oriented C++ toolkit SPDroot. It is based on the FairRoot framework initially developed for the FAIR experiments at GSI Darmstadt and partially compatible with MPDroot and BM@Nroot software used at MPD and BM@N, respectively.

The SPD detector description for Monte Carlo simulation is based on the ROOT geometry while transportation of secondary particles through material of the setup and simulation of detector response is provided by GEANT4 code. The standard multipurpose generators like Pythia6 and Pythia8 as well as specialised generators can be used for simulation of primary nucleon-nucleon collision. An example of p-p collision event in the SPD detector visualised by the SPDroot event viewer is shown in Fig. 35

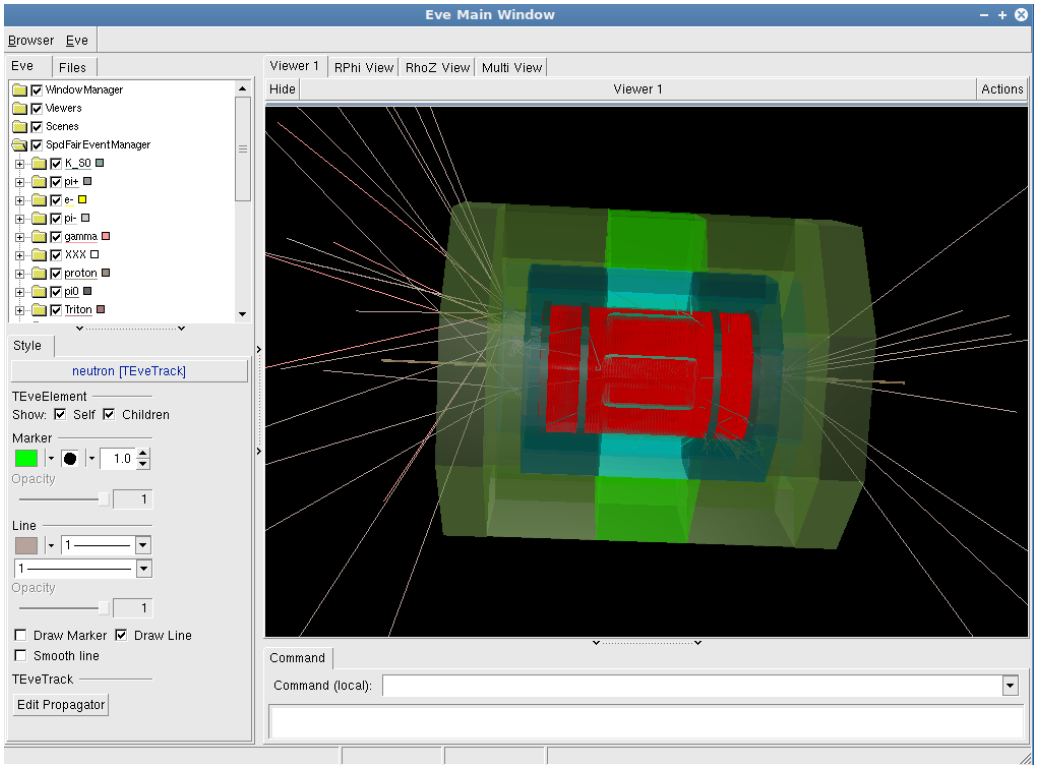

Figure 35: Event viewer of the SPDroot.

8 MC simulation and physics performance

8.1 Rates and spectra for minimum bias events

A collision of two beam particles at the interaction point creates certain number of secondary charged and neutral particles in the SPD setup. Table 2 shows the total cross section of p-p collisions, charged and neutral multiplicity of secondary particles for three collision energies. Angular and momentum distributions for different particles produced in the primary vertex of the p-p interactions at $\sqrt{s} = 26\ GeV$ is presented in Figure 36.

Table 2: Total cross section and average multiplicity at the vertex for charged and neutral particles in pp collisions as function of $\sqrt{s}$.

$\sqrt{s}$, GeV	σ_{tot}, mb	Charged multiplicity	Neutral (only γ) multiplicity
13	38.4	5.9	4.6 (3.8)
20	38.9	7.2	6.0 (5.0)
26	39.7	7.8	6.5 (5.5)

Secondary particles are produced in the interaction of primary particles with elements of the setup. The material budget between the interaction point and the closest internal surface of the ECal in average amounts to 0.15 X_0 or 0.03 λ_I. The average energy deposition in the ECal per one minimum bias event at $\sqrt{s} = 26\ GeV$ is 2.0 GeV in the Barrel (1.2 GeV from charged particles and 0.8 GeV from photons) and 5.0 GeV in each of the end-caps (3.7 GeV from charged particles and 1.3 GeV from photons).

8.2 Rates, spectra, background, etc. for processes of interest

8.2.1 Drell-Yan pair production

The general-purpose MC generators like PYTHIA produce only unpolarized Drell–Yan pairs. In [20, 36] a generator of polarized Drell–Yan pairs was developed. By using this generator we have generated two sets of simulated data corresponding to statistics of 10^5 and 5×10^4 events with Drell-Yan pairs for each of the following ranges of the photon virtuality Q^2, i.e. the lepton pair invariant mass squared: $2 < Q^2 < 8.5 GeV^2$ and $Q^2 > 11 GeV^2$. We have chosen these intervals in the invariant mass in order to escape low mass region with high probability for false identification of a lepton pair produced in various background processes (combinatorial background from Dalitz decays and γ conversion, etc.) like a Drell-Yan one and also to cut out the J/ψ region. Results for Sivers and Boer-Mulders asymmetries are shown in Figures 37 and 38, respectively.

As it is seen, even for relatively low statistics of 50 K of events with a Drell–Yan pair there are a few points, where the asymmetries exhibit measurable values of 4–6%. With statistics of 100 K events even the x_F dependence of the respective asymmetry could be reconstructed.

8.2.2 Physics with prompt photons

8.2.2.1 Signal and background Gluon Compton scattering (GCS) is the main mechanism of the prompt-photon production at SPD energies. At $\sqrt{s} = 26$ GeV the corresponding cross section calculated in the leading order is 1.2 μb. Contribution of the competitive quark-antiquark annihilation process is one order of magnitude smaller. Nevertheless, the main source of photons in hadronic collisions is the decay of secondary particles, mainly 2γ decays of π^0 and η mesons. Contributions of photons from the decays of different secondary particles are presented in Tab. 3. The p_T spectra of the GCS photons and of the decay photons produced near the interaction point are shown in Fig. 39. The contribution of the

decay photons dominates over the GCS signal everywhere , but the relative fraction of the signal photons increases with increasing of the p_T. The rejection of photons from reconstructed 2γ decays of π^0 and η-mesons and subsequent Monte Carlo-based statistical subtraction of the residual background photons is the only way to access the prompt-photon production, presumably at high p_T.

Another important source of background photons is the interaction of the secondary particles with the material of the detector elements. In addition, misidentification of "charged" energy clusters as "neutral" ones in the ECal due to inefficiency of the track finding and reconstruction algorithms produces additional contribution to the background rate. Overlapping of clusters produced by different particles could also contribute to the background via distortion of reconstructed kinematics.

Table 3: Contributions of photons from decays of different secondary particles (per event).

Decay	Number of photons
π^0	8.70
η	0.40
ω	0.06
η'	0.05
Σ^0	0.04
Others	0.01

8.2.2.2 Performance requirements for the SPD setup For successful realization of the prompt-photon program the SPD setup and especially the ECal have to meet the following requirements:

- inner space of the SPD setup should contain as minimal amount of material as possible in order to keep high transparency of the setup for photons;
- minimal tracking capability should be provided in order to distinguish between charged and neutral clusters in ECAL;
- reasonable granularity of the ECAL in order to avoid the pile-up effect that reduces the photon reconstruction efficiency and distorts kinematics of reconstructed photons;
- ability to detect with reasonable resolution an energy deposit down to 100 MeV to keep high reconstruction efficiency for photons. It is important to note that this threshold is significantly below the MIP signal ($\sim$ 200 MeV). Figure 39(b) shows the efficiency of the $\pi^0 \to \gamma\gamma$ decay reconstruction for different cluster energy thresholds and different granularities of the ECAL.

The invariant mass spectrum of two photons reconstructed in the ECal with 100 MeV and 500 MeV energy threshold is shown in Fig. 40(a). Relative energy resolution of the ECAL was assumed to be $dE/E = 1\% + 3.8\%/\sqrt{E}$. The Gaussian widths of the π^0 peaks is 5.7 MeV/c^2 and 3.6 MeV/c^2 for 100 MeV and 500 MeV thresholds, respectively. Figure 40(b) shows the p_T distribution of the GCS photons vs. x_F.

8.2.2.3 Expected accuracy for asymmetries A_N and A_{LL} Below we have roughly estimated the expected accuracy of the prompt-photon production cross-section and respective asymmetries A_N and A_{LL} measurements, based on the following simplifications. Data sample corresponds to 10^7 s of data taking (about 100 days) with average luminosity $L = 10^{32}\ s^{-1}cm^{-2}$. The inefficiency of the photon reconstruction is caused only by the geometrical acceptance and material distribution, no threshold for photon reconstruction in the ECal is applied. Leading order calculations are used for the GCS cross-section. Only the $\pi^0 \to \gamma\gamma$ decay is taken into account as a background. Average π^0 reconstruction

efficiency is 75.3%. Relative accuracy of the Monte Carlo description of the photon reconstruction efficiency is 1%. Two subsamples with equal statistics are collected with each combination of spin orientations. Absolute polarization of the beam is assumed to be exactly equal to 100%.

Since low-p_T region is useless for any studies of prompt photons due tothe huge background, while at high-p_T the statistics is very limited, a reasonable cut on the transverse momentum of a photon has to be applied in order to maximize the accuracy of the planned measurements. For the conditions mentioned above the optimal value lies around 5–6 GeV/c (see Figure 40(b). The total number of the detected GCS photons with $p_T > 5$ GeV/c is expected to be about 6×10^6.

The expected accuracy of the A_N and A_{LL} measurement in each of the four intervals in x_F in the range from -0.89 to 0.89 is shown in Fig 41. It is seen that we could distingush from zero asymmetries as low as $\geq 1\%$.

8.2.3 Charmonia reconstruction

The muon identification system of the SPD detector provides nice possibility to access the J/ψ and ψ' signals via their decays into a dimuon pair (branching fractions of 5.96% and 0.8%, respectively). ψ' could also be accessed via the decay into $J/\psi\pi^+\pi^-$ which has much higher branching fraction of 34.67%. The charmonia states $\chi_{c0,1,2}$ could be reconstructed, too, via detection in the ECal of the photon from the decay $\chi_{c0,1,2} \to J/\psi\gamma$.

8.2.3.1 Kinematic distributions, reconstruction efficiency and expected statistics The gluon-gluon fusion $gg \to J\psi g$ is the main mechanism of the J/ψ production at the NICA energies. Its contribution to the total production cross section in the leading order approximation is of about 20 nb. Figure 42(a) shows the momentum distribution for muons produced in the J/ψ decay. Figure 42(b) represents the expected muon identification efficiency, where the muon reached the Range System is counted as identified, as a function of the muon momentum. The efficiency drop at low momenta is due to the absorption of the soft muons in the material of the ECal. The momentum distribution for J/ψ produced in the gluon-gluon fusion hard process and the J/ψ reconstruction efficiency in the dimuon decay mode as a function of the J/ψ momentum are shown in Figure 43(a) and (b), respectively. The $J/\psi \to \mu^+\mu^-$ decay is supposed to be reconstructed if both muons have reached the Range System. The muon identification efficiency averaged over the muon spectrum and the J/ψ reconstruction efficiency averaged over the J/ψ spectrum are 96.5% and 93%, respectively. Figure 44 shows the p_T and x_F distributions for reconstructed J/ψ.

The main mechanisms of the $\chi_{c0,1,2}$ production are summarized in the Table 4 together with the cross sections (according to the NRQCD predictions). Since the particles have similar masses the kinematics of their decays $\chi_{c0,1,2} \to J/\psi\gamma$ is also similar. The spectrum of photons produced in the decay of the $\chi_c 2$ state (as the most intensive one) together with the reconstruction efficiency is shown in Fig. 45. The overall efficiency of the $\chi_{c0,1,2} \to J/\psi\gamma$ decay reconstruction is practically the same for all 3 states and equals to ≈80%. A 100 MeV photon reconstruction threshold was assumed.

Table 4: $\chi_{c0,1,2}$ properties.

State	M, MeV/c^2	Γ, MeV/c^2	$B_{J/\psi\gamma}$, %	Main production mechanisms
χ_{c0}	3414.71±0.30	10.8±0.6	1.40±0.05	$gg \to \chi_{c0}$ $gg \to \chi_{c0}g$
χ_{c1}	3510.67±0.05	0.84±0.04	34.3±1.0	$gg \to \chi_{c1}$
χ_{c2}	3556.17±0.07	1.97±0.09	19.0±0.5	$gg \to \chi_{c2}$ $gg \to \chi_{c2}g$

Our estimation of the expected statistics after 100 days of data taking is based on the J/ψ production cross section result $\sigma_{J/\psi} = 152 \pm 20$ nb at $\sqrt{s} = 24.3$ GeV from [92] and on the measurement of the ratio $R = \sigma_{\chi_{c1,2}} \times B_{\chi_c 1,2 \to J/\psi\gamma}/\sigma_{J/\psi} = 0.30 \pm 0.04$ at $\sqrt{s} = 23.761$ GeV from [93]. It results in $(8.4 \pm 1.1) \times 10^6$ of $J/\psi \to \mu^+\mu^-$ events and $(2.5 \pm 0.5) \times 10^6$ of $\chi_{c0,1,2} \to J/\psi\gamma \to \mu^+\mu^-\gamma$ events. Using the value of the ψ' production cross section from [94] $\sigma_{\psi'} = 28.9 \pm 11.3$ nb and assuming the same identification efficiency for the muons from the decay $\psi' \to \mu^+\mu^-$ we estimate the statistics of $\psi' \to \mu^+\mu^-$ and $\psi' \to J/\psi\pi^+\pi^- \to \mu^+\mu^-\pi^+\pi^-$ decays to be $(0.22 \pm 0.09) \times 10^6$ and $(0.55 \pm 0.22) \times 10^6$ events, correspondingly.

8.2.3.2 Expected background There are several sources of background processes that would complicate the J/ψ observation in the dimuon channel: i) combinatorial background; ii) open charm background where the muons come from the decays of D-mesons, iii) Drell-Yan pair production, iv) combinatorial background where false muon pair is reconstructed from muons originated from the decays of secondary pions. The last source is expected to be the dominant one.

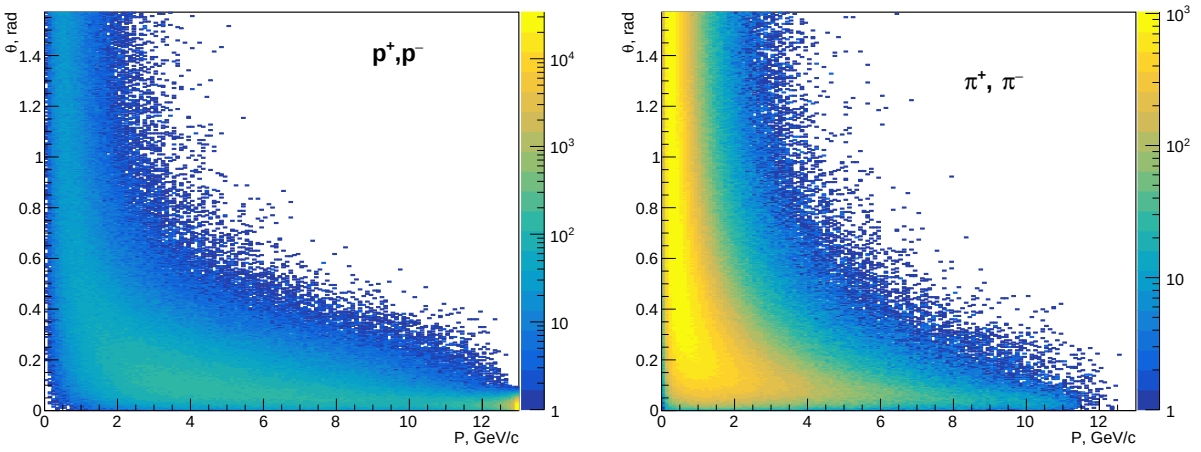

(a)

(b)

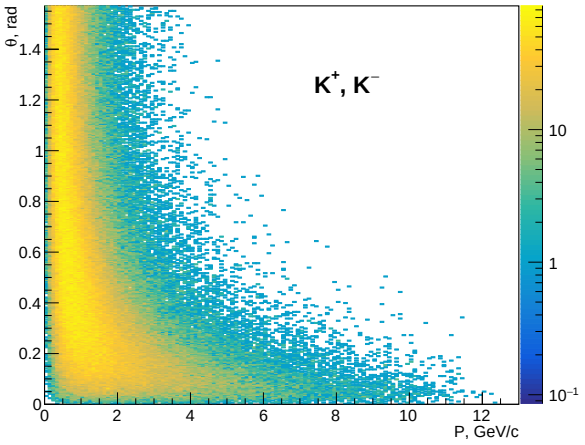

(c)

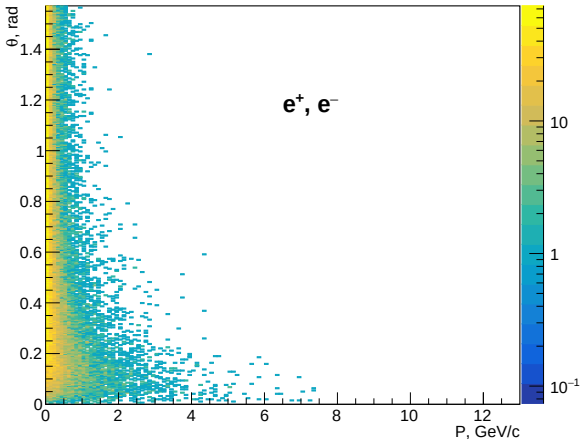

(d)

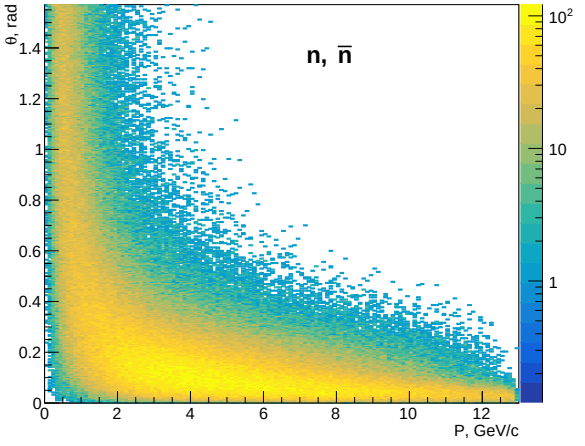

(e)

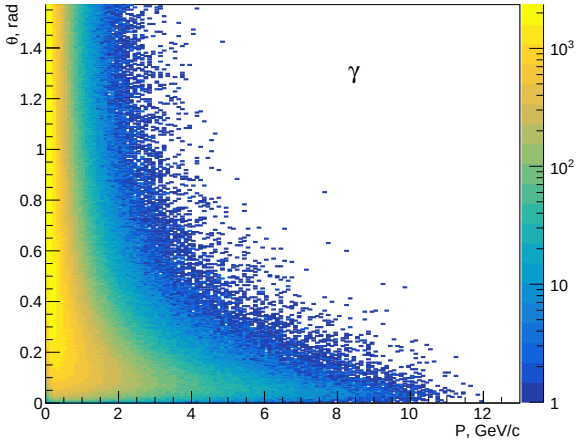

(f)

Figure 36: Momentum and angular distributions for particles produced in the primary vertex of p-p interactions at $\sqrt{s} = 26\ GeV$: $p^{\pm}$ (a), $\pi^{\pm}$ (b), $K^{\pm}$ (c), $e^{\pm}$ (d), n and $\bar{n}$ (e) and γ (f) per 10^6 minimum bias events.

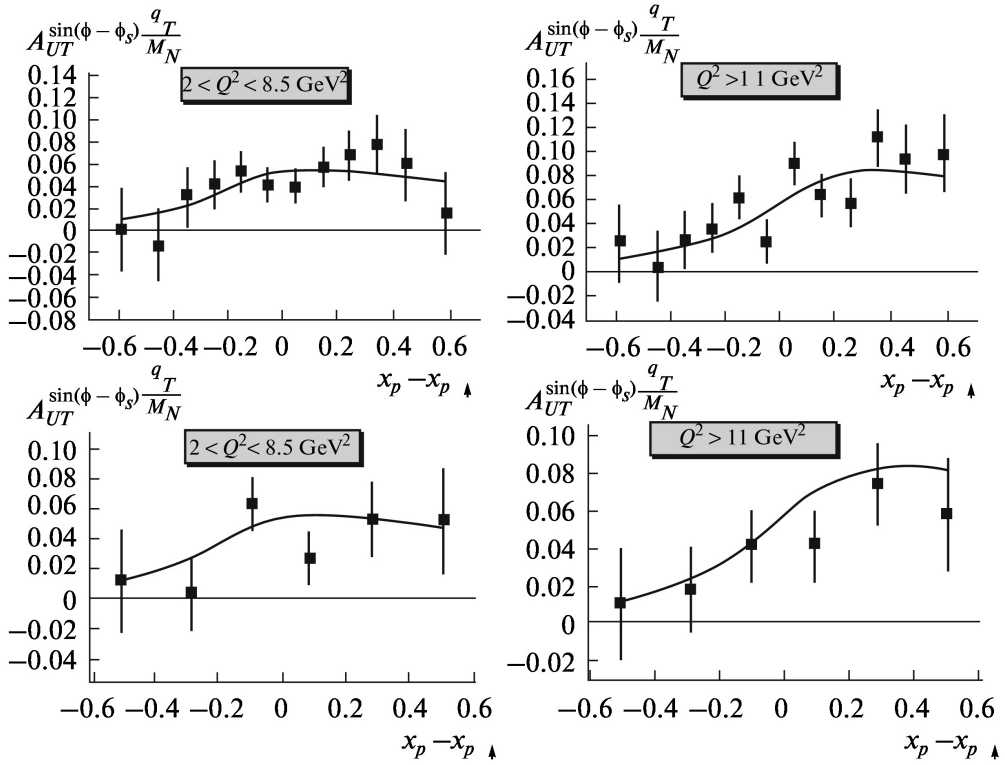

Figure 37: Simulated Sivers asymmetry of Drell-Yan pair production at NICA energies, $s = 400 GeV^2$ and in indicated intervals of photon virtuality Q^2. The results for the high statistical sample (10^5 events) are shown in the upper row, for the low statistics one (5×10^4 events) - in the lower row. The function fitted to the MC data is taken from [38].

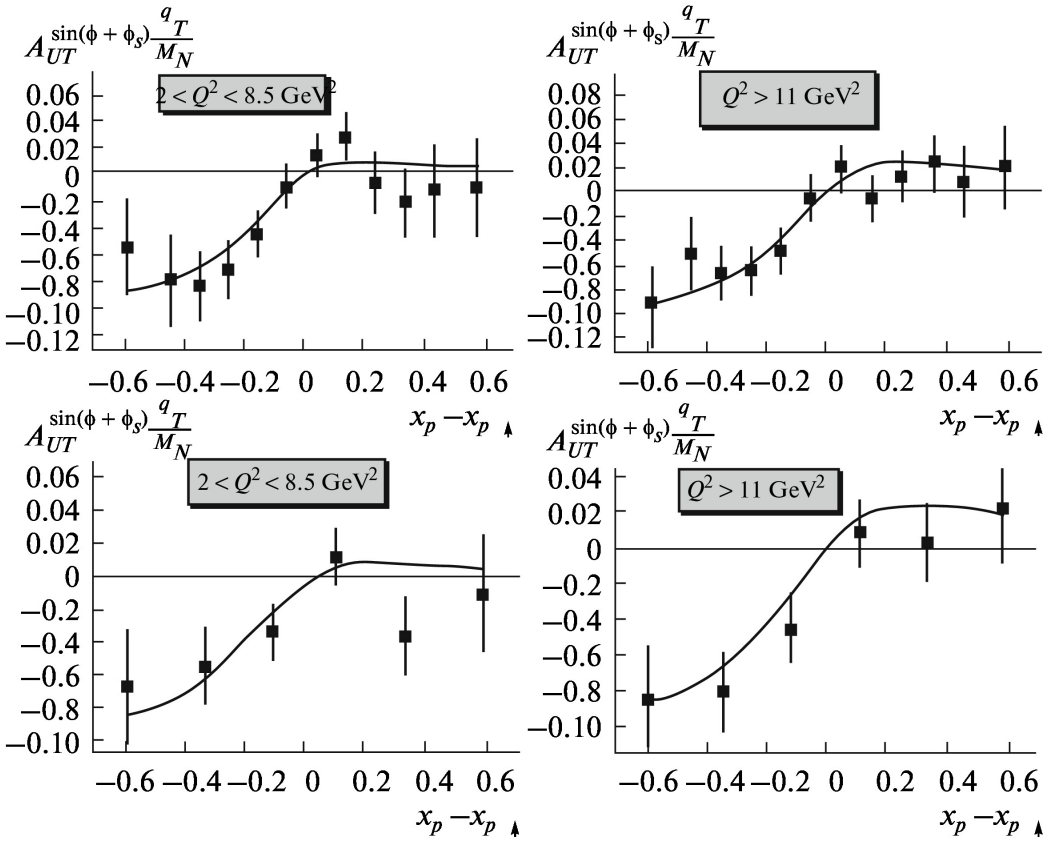

Figure 38: Simulated Boer-Mulders asymmetry of Drell-Yan pair production at NICA energies, $s = 400GeV^2$ and in indicated intervals of photon virtuality Q^2. The results for the high statistical sample (10^5 events) are shown in the upper row, for the low statistics one (5×10^4 events) - in the lower row.

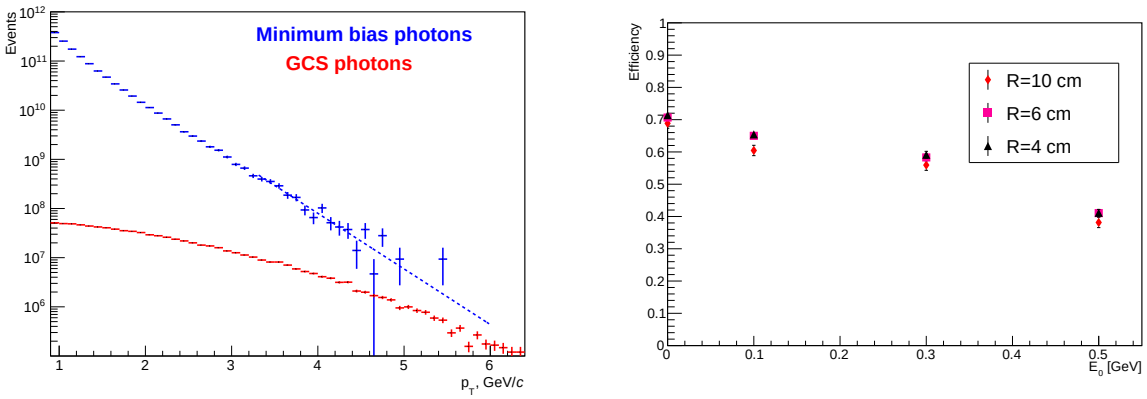

(a) (b)

Figure 39: (a) The p_T spectra of GCS prompt photons (red) and photons produced from π^0 decay (blue). (b) The efficiency of the $\pi^0 \to \gamma\gamma$ decay reconstruction in the case when at least one photon has $p_T > 2$ GeV/c as a function of cluster energy threshold for different granularities R of the ECal.

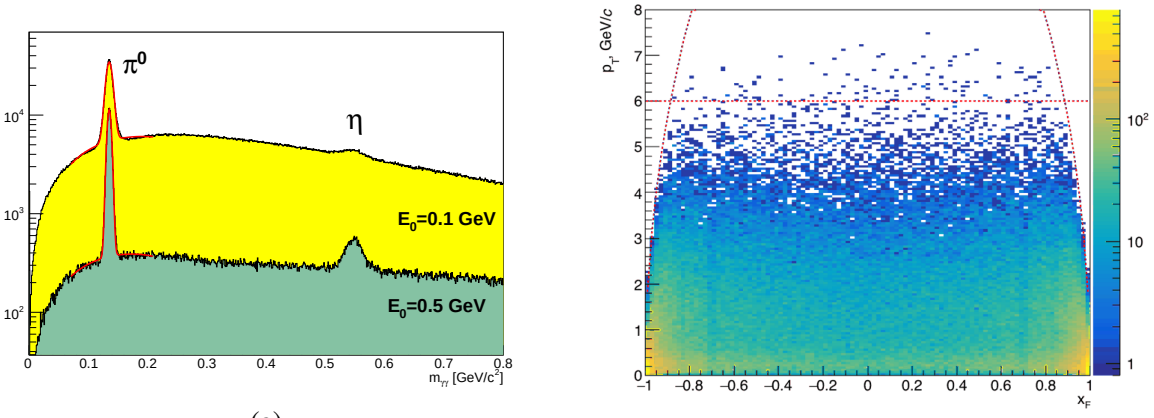

(a) (b)

Figure 40: (a) Invariant mass spectrum of two photons for two ECal thresholds: 100 MeV (yellow) and 500 MeV (green). (b) p_T distribution for GCS photons vs. x_F.

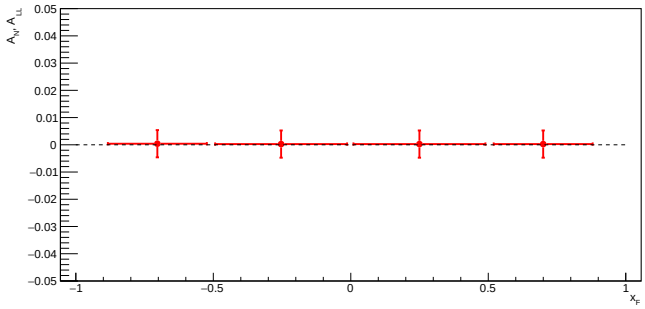

Figure 41: Expected accuracy of measured A_N and A_{LL} as function of x_F.

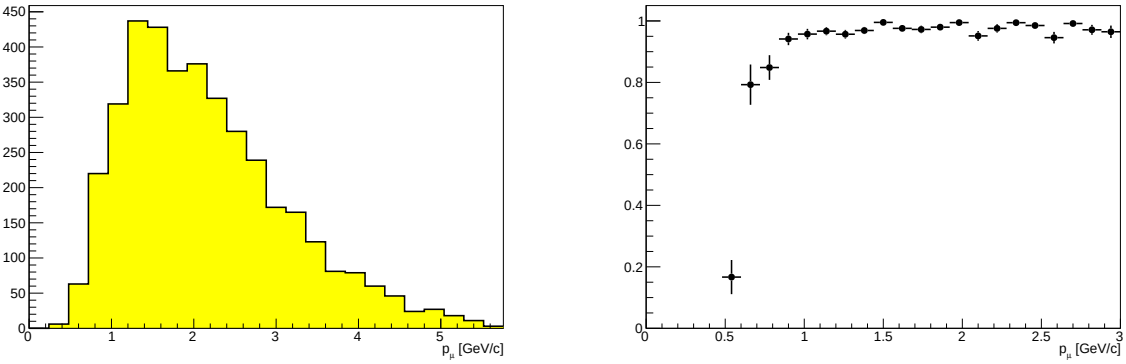

(a) (b)

Figure 42: (a) Momentum distribution for muons produced from the J/ψ decay. (b) Muon identification efficiency as a function of muon momentum.

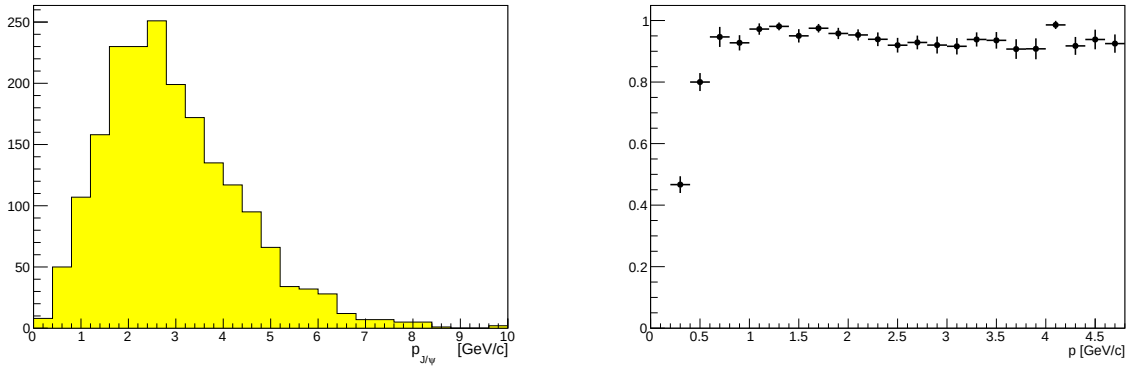

(a) (b)

Figure 43: (a) Momentum distribution for J/ψ produced in the gluon-gluon fusion hard process (b) J/ψ reconstruction efficiency as a function of the J/ψ momentum.

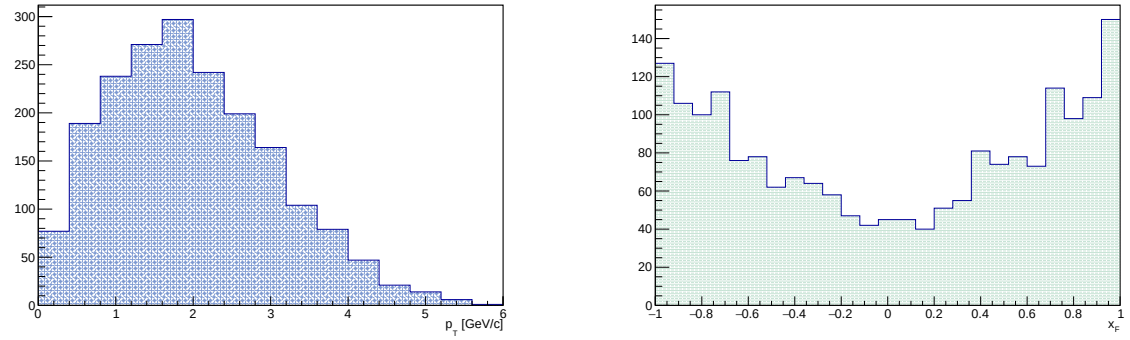

(a) (b)

Figure 44: p_T (a) and x_F (b) distributions for the reconstructed J/ψ.

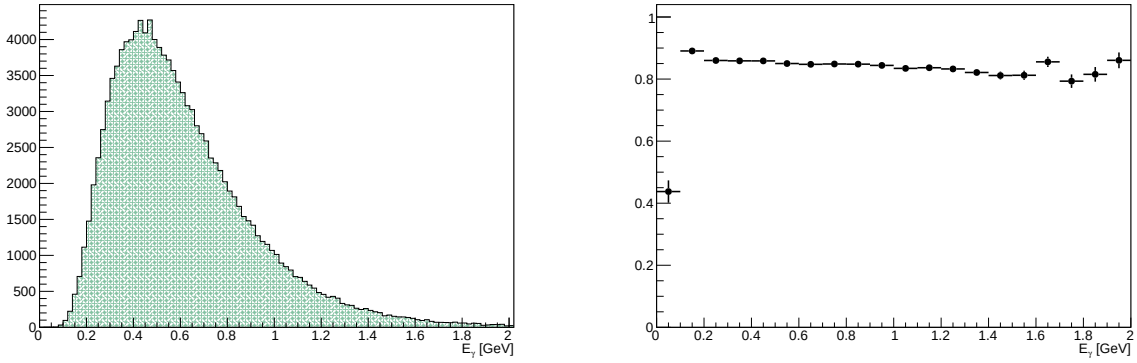

(a) (b)

Figure 45: (a) Spectrum of photons produced in the decay of the χ_{c2}. (b) Reconstruction efficiency for the photon from the $\chi_{c2} \to J/\psi\gamma$ decay.

9 Participating institutions and author list

Host institute of the project is the Laboratory of High-Energy Physics of the Joint Institute for Nuclear Research. The main part of the human resources engaged with the project comes from there (74 researchers, 24.4 FTE). The Laboratory of Nuclear Problems is the other laboratory of the JINR that participates in the project with substantial number of researchers (30 researchers, 11.3 FTE). Altogether the JINR engagement in the project now evaluates to 37.7 full-time-equivalent (FTE) researchers.

Fourteen institutes from the JINR Member States and other countries have expressed by now their interest for participation in the project and indicate that they could allocate resources and manpower for the project. The list of institutes together with the names of researchers (in some cases only the leaders of the teams are listed) is given below. Received Expressions of Interest are collected under a separate cover.

Institute of Applied Physics of the National Academy of Sciences of Belarus, Minsk, Belarus

Shulyakovsky R.

Higher Institute of Technologies and Applied Sciences (InSTEC), Havana University, Havana, Cuba

Guzman F., Garsía Trapaga C.E.

Charles University, Prague, Czech Republic

Finger M., Finger M. (jr.), Hrusovsky J., Jandek M., Prochazka I., Slunecka M., Sluneckova V., Stepankova H., Zemko M.

Czech Technical University in Prague, Czech Republic

Jary V., Lednicky D., Marcisovsky M., Neue G., Novy J., Popule J., Virius M., Vrba V.

University of Turin and INFN Section, Turin, Italy

Denisov O.Yu., Panzieri D., Rivetti A.

Joint Institute for Nuclear Research, JINR, Dubna, Russia

Directorate

Lednický R.

Laboratory of High-Energy Physics

Anosov V.A., Akhunzyanov R.R., Azorskiy N.I., Baldin A.A., Baldina E.G., Barabanov M.Yu., Beloborodov A.N., Dunin V.B., Enik T.L., Filatov Yu.N., Gavrishchuk O.P., Galoyan A.S., Gribovsky A.S., Gromov V.A., Gurchin Yu.V., Gusakov Yu.V., Ivanov A.V., Ivanov N.Ya., Isupov A.Yu., Kekelidze G.D., Khabarov S.V., Kharusov P.R., Kovalenko A.D., Kovalev Yu.S., Kozhin M.A., Kolesnikov A.O., Kokoulina E.S., Kopylov Yu.A., Kostukov E.V., Kramarenko V.A., Khrenov A.N., Kruglov V.N., Kuzmin N., Ladygin E., Ladygin V.P., Lapshina I.V., Lysan V.M., Makankin A.M., Meshcheriakov G.V., Moshkovsky I.V., Nagaitsev A.P., Nagorniy S., Nikitin V.A., Pavlov V.V., Paraipan M., Parzhitskii S.S., Perepelkin E.E., Petukhov Yu., Peshekhonov D.V., Reznikov S.G., Rogachevsky O.V., Savenkov A.A., Sheremeteva A.I., Shimanskii S.S., Skhomenko Ya.T., Starikova S.Yu., Streletskaya E.A., Tarasov O.G., Tarasova L.N., Teryaev O.V., Tishevsky A.V., Topilin N.D., Topko B.L., Tsenov R., Usenko E.A., Vasilieva E.V., Veselova N.I., Volkov P.V., Yudin I.P., Zamyatin N.I., Zemlyanichkina E.V., Zhukov I.A., Zinin A.V., Zubarev E.V.

Laboratory of Nuclear Problems

Abazov V.M., Alexeev G.D., Afanasyev L.G., Denisenko I.I., Duginov V.N., Fedorov A.N., Frolov V.N., Golovanov G.A., Gritsay K. I., Guskov A.V., Komarov V.I., Kulikov A.V., Kutuzov S.A., Nefedov Yu.A., Piskun A.A., Prokhorov I.K., Romanov V.M., Rudenko A.I., Rymbekova A., Samartsev A.G., Semenov A.V., Skachkov N.B., Skachkova A.N., Tsirkov D.A., Tkachenko A.V., Tokmenin V.V., Uzikov Yu. N., Verkheev A.Yu., Vertogradov L.S., Zhuravlev N.F.

Laboratory of Theoretical Physics
Anikin I.V., Efremov A.V.,Goloskokov S.V., Klopot Ya., Strusik-Kotlozh D., Volchansky N.I.

Laboratory of Information Technologies
Uzhinsky V.V.

St. Petersburg Nuclear Physics Institute, Gatchina, Russia
Kim V.T.

Lebedev Physical Institute of the Russian Academy of Sciences, Moscow, Russia
Andreev V.F., Baskov V.A., Dalkarov O.D., Gerassimov S.G., L'vov A.Yo., Negodaev M.A., Nechaeva P.Yu., Polyanskiy V.V., Soutchkov S.I., Terkulov A.R., Topchiev N.P.

Skobeltsin Institute of Nuclear Physics of the Moscow State University, Moscow, Russia
Boos E., Chepurnov A., Merkin M., Nikolaev A.

Institute for Theoretical and Experimental Physics, Moscow, Russia
Akindinov A.V., Alekseev, Golubev A., Kirin D.Yu., Luschevskaya E., Malkevich D.B., B. Morozov, Plotnikov V.V., Polozov P., Rusinov V., Stavinskiy A.V., Sultanov R.I., D. Svirida, Tarkovskyi E.I., Zhigareva N.M.

Institute for High-Energy Physics, Protvino, Russia
Vorobiev A.

Samara National Research University, Samara, Russia
A.V. Karpishkov, M.A. Nefedov, V.A. Saleev, A.V. Shipilova

St. Petersburg Polytechnic University, St. Petersburg, Russia
Berdnikov Ya.

St. Petersburg State University, St. Petersburg, Russia
Feofilov G.A., V.Kovalenko V.N., Valiev F.F., Vechernin V.V., Zherebchevsky V.Yo.

Tomsk State University, Tomsk, Russia
Burtsev V., Chumakov A., Dusaev R., Lyubovitskij V., Mamon S., Sharko K., Trifonov A., Vasilishin B., Zhevlakov A.

10 Project time-line

We propose a three-year project for delivering of a technical design of the start-up configuration of the SPD facility based on the necessary simulation work, prototypes construction and test measurements.

The time-line is seen as follows:

- submission of a JINR project for design of the SPD facility for the PAC meeting in January 2019;
- setting up of the SPD collaboration and election of its management bodies (2019);
- signing of MoU (2019);
- preparation of Conceptual Design Report and submission to the PAC by the end of 2019;
- Preparation of Technical Design Report for the start-up configuration of the facility, including prototyping and test measurements (2020 – 2021);

We hope to be able to start construction of the first stage of the detector in 2022 and perform first measurements somewhere in 2025.

References

[1] S. D. Drell, T.-M. Yan, Massive Lepton Pair Production in Hadron-Hadron Collisions at High-Energies, Phys. Rev. Lett. 25 (1970) 316–320, [Erratum: Phys. Rev. Lett.25,902(1970)]. (Cited in Sec. 1.)

[2] S. D. Drell, T.-M. Yan, Partons and their Applications at High-Energies, Annals Phys. 66 (1971) 578, [Annals Phys.281,450(2000)]. (Cited in Sec. 1.)

[3] G. T. Bodwin, Factorization of the Drell-Yan Cross-Section in Perturbation Theory, Phys. Rev. D31 (1985) 2616, [Erratum: Phys. Rev.D34,3932(1986)]. (Cited in Sec. 1.)

[4] J. C. Collins, D. E. Soper, G. F. Sterman, Factorization for Short Distance Hadron - Hadron Scattering, Nucl. Phys. B261 (1985) 104–142. (Not cited.)

[5] J. C. Collins, D. E. Soper, G. F. Sterman, Soft Gluons and Factorization, Nucl. Phys. B308 (1988) 833–856. (Not cited.)

[6] J. C. Collins, D. E. Soper, G. F. Sterman, Factorization of Hard Processes in QCD, Adv. Ser. Direct. High Energy Phys. 5 (1989) 1–91. (Cited in Sec. 1.)

[7] J. C. Collins, What exactly is a parton density?, Acta Phys. Polon. B34 (2003) 3103. (Cited in Sec. 1.)

[8] J. C. Collins, T. C. Rogers, A. M. Stasto, Fully unintegrated parton correlation functions and factorization in lowest-order hard scattering, Phys. Rev. D77 (2008) 085009. (Cited in Sec. 1.)

[9] D. Boer, P. J. Mulders, Time reversal odd distribution functions in leptoproduction, Phys. Rev. D57 (1998) 5780–5786. (Cited in Sec. 1.)

[10] D. W. Sivers, Single Spin Production Asymmetries from the Hard Scattering of Point-Like Constituents, Phys. Rev. D41 (1990) 83. (Not cited.)

[11] D. W. Sivers, Hard scattering scaling laws for single spin production asymmetries, Phys. Rev. D43 (1991) 261–263. (Cited in Sec. 1.)

[12] J. C. Collins, D. E. Soper, Back-To-Back Jets in QCD, Nucl. Phys. B193 (1981) 381, [Erratum: Nucl. Phys.B213,545(1983)]. (Cited in Sec. 1.)

[13] J. C. Collins, A. Metz, Universality of soft and collinear factors in hard-scattering factorization, Phys. Rev. Lett. 93 (2004) 252001. (Not cited.)

[14] X.-d. Ji, J.-p. Ma, F. Yuan, QCD factorization for semi-inclusive deep-inelastic scattering at low transverse momentum, Phys. Rev. D71 (2005) 034005. (Not cited.)

[15] X.-d. Ji, J.-P. Ma, F. Yuan, QCD factorization for spin-dependent cross sections in DIS and Drell-Yan processes at low transverse momentum, Phys. Lett. B597 (2004) 299–308. (Cited in Sec. 1.)

[16] G. Bunce, et al., Plans for the RHIC Spin Physics Program, http://spin.riken.bnl.gov/rsc/report/spinplan_2008/spinplan08.pdf, see also arXiv:1501.01220 . (Cited in Sec. 1.)

[17] J. C. Peng, S. Sawada, et al., J-PARC Proposal P04, http://j-parc.jp/NuclPart/pac_0606/pdf/p04-Peng.pdf . (Cited in Sec. 1.)

[18] Y. Goto, H. Sato, et al., J-PARC Proposal P24, http://j-parc.jp/NuclPart/pac_0801/pdf/Goto.pdf . (Cited in Sec. 1.)

[19] V. V. Abramov, et al., Spin physics program in the U70 polarized proton beam, in: 11th International Workshop on High Energy Spin Physics (DUBNA-SPIN-05) Dubna, Russia, September 27-October 1, 2005, 2005. (Cited in Sec. 1.)

[20] A. Sissakian, O. Shevchenko, A. Nagaytsev, O. Ivanov, Transversity and T-odd PDFs from Drell-Yan processes with p p, p D and D D collisions, Eur. Phys. J. C59 (2009) 659–673. (Cited in Secs. 1, 2.2 and 8.2.1.)

[21] I. A. Savin, et al., Spin Physics Experiments at NICA-SPD with polarized proton and deuteron beams, https://arxiv.org/abs/1408.3959, (2014), EPJ Web Conf. 85 (2015) 02039. (Cited in Secs. 1, 2.2, 2.2 and 4.1.)

[22] V. Barone, et al., Antiproton-proton scattering experiments with polarization, https://arxiv.org/abs/hep-ex/0505054, (2005) . (Cited in Sec. 1.)

[23] G. Baum, et al., COMPASS: A Proposal for a Common Muon and Proton Apparatus for Structure and Spectroscopy, CERN-SPSLC-96-14, CERN-SPSLC-P-297, (1996) . (Cited in Sec. 1.)

[24] P. Aurenche, M. Fontannaz, J.-P. Guillet, E. Pilon, M. Werlen, A New critical study of photon production in hadronic collisions, Phys. Rev. D73 (2006) 094007. (Cited in Secs. 1, 2.3 and 5.)

[25] D. Boer, C. Lorcé, C. Pisano, J. Zhou, The gluon Sivers distribution: status and future prospects, Adv. High Energy Phys. 2015 (2015) 371396. (Cited in Secs. 1 and 2.3.)

[26] S. Arnold, A. Metz, M. Schlegel, Dilepton production from polarized hadron hadron collisions, Phys. Rev. D79 (2009) 034005. (Cited in Sec. 2.2.)

[27] L. P. Gamberg, D. S. Hwang, A. Metz, M. Schlegel, Light-cone divergence in twist-3 correlation functions, Phys. Lett. B639 (2006) 508–512. (Not cited.)

[28] A. Bacchetta, D. Boer, M. Diehl, P. J. Mulders, Matches and mismatches in the descriptions of semi-inclusive processes at low and high transverse momentum, JHEP 08 (2008) 023. (Not cited.)

[29] M. Anselmino, M. Boglione, U. D'Alesio, S. Melis, F. Murgia, A. Prokudin, Sivers effect and the single spin asymmetry A_N in $p^\uparrow p \to hX$ processes, Phys. Rev. D88 (5) (2013) 054023. (Not cited.)

[30] D. Boer, L. Gamberg, B. Musch, A. Prokudin, Bessel-Weighted Asymmetries in Semi Inclusive Deep Inelastic Scattering, JHEP 10 (2011) 021. (Not cited.)

[31] P. J. Mulders, R. D. Tangerman, The Complete tree level result up to order 1/Q for polarized deep inelastic leptoproduction, Nucl. Phys. B461 (1996) 197–237, [Erratum: Nucl. Phys.B484,538(1997)]. (Not cited.)

[32] A. Bacchetta, M. Diehl, K. Goeke, A. Metz, P. J. Mulders, M. Schlegel, Semi-inclusive deep inelastic scattering at small transverse momentum, JHEP 02 (2007) 093. (Cited in Sec. 2.2.)

[33] A. Sissakian, O. Shevchenko, O. Ivanov, On duality of Drell-Yan and J/psi production processes, Pisma Zh. Eksp. Teor. Fiz. 86 (2007) 863–867, [JETP Lett.86,751(2007)]. (Cited in Sec. 2.2.)

[34] A. N. Sissakian, O. Yu. Shevchenko, A. P. Nagaytsev, O. N. Ivanov, Direct extraction of transversity and its accompanying T-odd distribution from the unpolarized and single-polarized Drell-Yan process, Phys. Rev. D72 (2005) 054027. (Not cited.)

[35] A. Sissakian, O. Shevchenko, A. Nagaytsev, O. Denisov, O. Ivanov, Transversity and its accompanying T-odd distribution from Drell-Yan processes with pion-proton collisions, Eur. Phys. J. C46 (2006) 147–150. (Not cited.)

[36] A. N. Sissakian, O. Yu. Shevchenko, A. P. Nagaitsev, O. N. Ivanov, Polarization effects in Drell-Yan processes, Phys. Part. Nucl. 41 (2010) 64–100. (Cited in Secs. 2.2 and 8.2.1.)

[37] A. V. Efremov, K. Goeke, S. Menzel, A. A. Metz, S. P., Sivers effect in semi-inclusive DIS and in the Drell-Yan process, Phys. Lett. B 612 (2004) 233–244. (Cited in Sec. 2.2.)

[38] J. C. Collins, A. V. Efremov, K. Goeke, S. Menzel, A. Metz, P. Schweitzer, Sivers effect in semi-inclusive deeply inelastic scattering, Phys. Rev. D73 (2006) 014021. (Cited in Secs. 2.2 and 37.)

[39] T. e. a. COMPASS Collaboration (M. Aghasyan (INFN, First measurement of transverse-spin-dependent azimuthal asymmetries in the Drell-Yan process, Phys.Rev.Lett. 119 (2017) no.11, 112002. (Cited in Sec. 2.2.)

[40] I. Schmidt, J. Soffer, J.-J. Yang, Transverse single spin asymmetries in photon production, Phys. Lett. B612 (2005) 258–262. (Cited in Sec. 2.3.)

[41] J.-w. Qiu, G. F. Sterman, Single transverse spin asymmetries in direct photon production, Nucl. Phys. B378 (1992) 52–78. (Cited in Secs. 2.3 and 6.)

[42] X.-D. Ji, Gluon correlations in the transversely polarized nucleon, Phys. Lett. B289 (1992) 137–142. (Cited in Sec. 2.3.)

[43] N. Hammon, B. Ehrnsperger, A. Schaefer, Single-transverse spin asymmetry in prompt photon production, J. Phys. G24 (1998) 991–1001. (Cited in Secs. 2.3 and 6.)

[44] L. Gamberg, Z.-B. Kang, Single transverse spin asymmetry of prompt photon production, Phys. Lett. B718 (2012) 181–188. (Cited in Sec. 2.3.)

[45] D. L. Adams, et al., Measurement of single spin asymmetry for direct photon production in p p collisions at 200-GeV/c, Phys. Lett. B345 (1995) 569–575. (Cited in Sec. 2.3.)

[46] H.-Y. Cheng, S.-N. Lai, Spin Asymmetry in Proton Proton Collisions as a Probe of Sea and Gluon Polarization in a Proton, Phys. Rev. D41 (1990) 91. (Cited in Sec. 2.3.)

[47] G. Bunce, N. Saito, J. Soffer, W. Vogelsang, Prospects for spin physics at RHIC, Ann. Rev. Nucl. Part. Sci. 50 (2000) 525–575. (Cited in Sec. 2.3.)

[48] R. Li, J.-X. Wang, Next-to-Leading-Order QCD corrections to $J/\psi(\upsilon)+\gamma$ production at the LHC, Phys. Lett. B672 (2009) 51–55. (Cited in Sec. 2.3.)

[49] J. P. Lansberg, Back-to-back isolated photon-quarkonium production at the LHC and the transverse-momentum-dependent distributions of the gluons in the proton, Int. J. Mod. Phys. Conf. Ser. 40 (2016) 1660015. (Cited in Sec. 2.3.)

[50] R. Vogt, The x(F) dependence of ψ and Drell-Yan production, Phys. Rev. C61 (2000) 035203. (Cited in Secs. 2.4 and 7.)

[51] N. Brambilla, et al., Heavy quarkonium: progress, puzzles, and opportunities, Eur. Phys. J. C71 (2011) 1534. (Cited in Secs. 2.4 and 2.4.2.)

[52] N. Brambilla, et al., QCD and Strongly Coupled Gauge Theories: Challenges and Perspectives, Eur. Phys. J. C74 (10) (2014) 2981. (Cited in Sec. 2.4.)

[53] G. T. Bodwin, E. Braaten, J. Lee, Comparison of the color-evaporation model and the NRQCD factorization approach in charmonium production, Phys. Rev. D72 (2005) 014004. (Cited in Sec. 2.4.)

[54] R. Gavai, D. Kharzeev, H. Satz, G. A. Schuler, K. Sridhar, R. Vogt, Quarkonium production in hadronic collisions, Int. J. Mod. Phys. A10 (1995) 3043–3070. (Cited in Sec. 2.4.)

[55] G. T. Bodwin, E. Braaten, G. P. Lepage, Rigorous QCD analysis of inclusive annihilation and production of heavy quarkonium, Phys. Rev. D51 (1995) 1125–1171, [Erratum: Phys. Rev.D55,5853(1997)]. (Cited in Sec. 2.4.)

[56] G. T. Bodwin, D. K. Sinclair, S. Kim, Quarkonium decay matrix elements from quenched lattice QCD, Phys. Rev. Lett. 77 (1996) 2376–2379. (Cited in Sec. 2.4.)

[57] M. Butenschoen, B. A. Kniehl, Next-to-leading-order tests of NRQCD factorization with J/ψ yield and polarization, Mod. Phys. Lett. A28 (2013) 1350027. (Cited in Sec. 2.4.)

[58] F. Maltoni, et al., Analysis of charmonium production at fixed-target experiments in the NRQCD approach, Phys. Lett. B638 (2006) 202–208. (Cited in Sec. 8.)

[59] M. Anselmino, V. Barone, A. Drago, N. N. Nikolaev, Accessing transversity via J / psi production in polarized p vector anti-p vector interactions, Phys. Lett. B594 (2004) 97–104. (Cited in Sec. 2.4.1.)

[60] E. Leader, E. Predazzi, AN INTRODUCTION TO GAUGE THEORIES AND THE 'NEW PHYSICS.', 1982. (Cited in Sec. 2.4.1.)

[61] V. Barone, Z. Lu, B.-Q. Ma, The cos 2 phi asymmetry of Drell-Yan and J/psi production in unpolarized p anti-p scattering, Eur. Phys. J. C49 (2007) 967–971. (Cited in Sec. 2.4.1.)

[62] C. Patrignani, et al., Review of Particle Physics, Chin. Phys. C40 (10) (2016) 100001. (Cited in Sec. 2.4.2.)

[63] M. Y. Barabanov, A. S. Vodopyanov, A. I. Zinchenko, S. L. Olsen, Perspective study of charmonium and exotics above the $d\bar{D}$ threshold, Physics of Atomic Nuclei 79 (1) (2016) 126–129. (Cited in Sec. 2.4.2.)

[64] M. Y. Barabanov, A. S. Vodopyanov, S. L. Olsen, New research of charmonium over $d\bar{D}$ threshold using the antiproton beam with momentum ranging from 1 to 15 gev/c, Physics of Atomic Nuclei 77 (1) (2014) 126–130. (Cited in Sec. 2.4.2.)

[65] S. V. Goloskokov, P. Kroll, The Longitudinal cross-section of vector meson electroproduction, Eur. Phys. J. C50 (2007) 829–842. (Cited in Sec. 2.5.)

[66] S. V. Goloskokov, P. Kroll, The Role of the quark and gluon GPDs in hard vector-meson electroproduction, Eur. Phys. J. C53 (2008) 367–384. (Cited in Sec. 2.5.)

[67] Y. Hagiwara, Y. Hatta, R. Pasechnik, M. Tasevsky, O. Teryaev, Accessing the gluon Wigner distribution in ultraperipheral pA collisions, Phys. Rev. D96 (3) (2017) 034009. (Cited in Sec. 2.5.)

[68] O. V. Teryaev, Analytic properties of hard exclusive amplitudes, in: 11th International Conference on Elastic and Diffractive Scattering: Towards High Energy Frontiers: The 20th Anniversary of the Blois Workshops, 17th Rencontre de Blois (EDS 05) Chateau de Blois, Blois, France, May 15-20, 2005, 2005. (Cited in Sec. 2.5.)

[69] S. V. Goloskokov, P. Kroll, O. V. Teryaev, in progress . (Cited in Sec. 2.5.)

[70] G. S. Atoian, V. V. Issakov, O. V. Karavichev, T. L. Karavicheva, A. A. Poblaguev, M. E. Zeller, Development of Shashlyk calorimeter for KOPIO, Nucl. Instrum. Meth. A531 (2004) 467–480. (Cited in Sec. 4.5.)

[71] V. M. Abazov, G. D. Alexeev, Y. I. Davydov, V. L. Malyshev, V. V. Tokmenin, A. A. Piskun, Comparative analysis of the performance characteristics of mini-drift tubes with different design, Instruments and Experimental Techniques 53 (3) (2010) 356–361. (Cited in Sec. 4.6.1.)

[72] V. M. Abazov, G. D. Alexeev, Y. I. Davydov, V. L. Malyshev, A. A. Piskun, V. V. Tokmenin, Coordinate accuracy of mini-drift tubes in detection of an induced signal, Instruments and Experimental Techniques 53 (5) (2010) 648–652. (Cited in Sec. 4.6.1.)

[73] V. M. Abazov, et al., The Muon system of the run II D0 detector, Nucl. Instrum. Meth. A552 (2005) 372–398. (Cited in Sec. 4.6.3.)

[74] P. Abbon, et al., The COMPASS experiment at CERN, Nucl. Instrum. Meth. A577 (2007) 455–518. (Cited in Sec. 4.6.3.)

[75] A. Akindinov, et al., RPC with low-resistive phosphate glass electrodes as a candidate for the CBM TOF, Nucl. Instrum. Meth. A572 (2007) 676–681. (Cited in Sec. 4.7.1.)

[76] V. Ammosov, et al., Performance of RPC with low-resistive silicate glass electrodes exposed to an intense continuous electron beam, Nucl. Instrum. Meth. A576 (2007) 331–336. (Not cited.)

[77] J. Wang, et al., Nucl. Instrum. Meth. A731 (2013) 40. (Cited in Sec. 4.7.1.)

[78] Y. Haddad, G. Grenier, I. Laktineh, N. Lumb, S. Cauwenbergh, High Rate Resistive Plate Chamber for LHC detector upgrades, Nucl. Instrum. Meth. A718 (2013) 424–426. (Cited in Sec. 4.7.1.)

[79] A. Akindinov, et al., Radiation-hard ceramic Resistive Plate Chambers for forward TOF and T0 systems, Nucl. Instrum. Meth. A875 (2017) 203. (Cited in Sec. 4.7.1.)

[80] V. A. Gapienko, O. P. Gavrishchuk, A. A. Golovin, A. A. Semak, S. Ya. Sychkov, Yu. M. Sviridov, E. A. Usenko, M. N. Ukhanov, Studying the counting rate capability of a glass multigap resistive plate chamber at an increased operating temperature, Instrum. Exp. Tech. 56 (2013) 265–270, [Prib. Tekh. Eksp.2013,no.3,21(2013)]. (Cited in Sec. 4.7.1.)

[81] M. Bondila, et al., Results of in-beam tests of an MCP-based vacuum sector prototype of the T0/centrality detector for ALICE, Nucl. Instrum. Meth. A478 (2002) 220–224. (Cited in Secs. 27 and 28.)

[82] T. Gys, Micro-channel plates and vacuum detectors, Nucl. Instrum. Meth. A787 (2015) 254–260. (Cited in Sec. 4.8.)

[83] B. Z. Kopeliovich, I. K. Potashnikova, I. Schmidt, J. Soffer, Single transverse spin asymmetry of forward neutrons, Phys. Rev. D84 (2011) 114012. (Cited in Sec. 29.)

[84] A. Adare, et al., Inclusive cross section and single transverse spin asymmetry for very forward neutron production in polarized p+p collisions at s=200 GeV, Phys. Rev. D88 (3) (2013) 032006. (Cited in Sec. 4.9.2.)

[85] D. L. Adams, et al., Comparison of spin asymmetries and cross-sections in pi0 production by 200 GeV polarized anti-protons and protons, Phys. Lett. B261 (1991) 201–206. (Cited in Secs. 4.9.3 and 30.)

[86] D. L. Adams, et al., Analyzing power in inclusive pi+ and pi- production at high x(F) with a 200-GeV polarized proton beam, Phys. Lett. B264 (1991) 462–466. (Cited in Secs. 4.9.3 and 30.)

[87] C. E. Allgower, et al., Measurement of analyzing powers of pi+ and pi- produced on a hydrogen and a carbon target with a 22-GeV/c incident polarized proton beam, Phys. Rev. D65 (2002) 092008. (Cited in Sec. 4.9.3.)

[88] D. Steffen, et al., Overview and Future Developments of the intelligent, FPGA-based DAQ (iFDAQ) of COMPASS, PoS ICHEP2016 (2016) 912. (Cited in Sec. 4.10.)

[89] M. Bodlak, V. Frolov, V. Jary, S. Huber, I. Konorov, D. Levit, J. Novy, R. Salac, M. Virius, Development of new data acquisition system for compass experiment, Nuclear and Particle Physics Proceedings 273-275 (2016) 976 – 981, 37th International Conference on High Energy Physics (ICHEP). (Cited in Sec. 4.10.)

[90] I. N. Meshkov, G. V. Trubnikov, et al., NICA Technical Desigh Report, Dubna, (2015) . (Cited in Sec. 6.)

[91] A. N. Sissakian, A. S. Sorin, V. D. Kekelidze, et al., The MultiPurpose Detector – MPD to study Heavy Ion Collisions at NICA (Conceptual Design Report), Dubna, (2014) . (Cited in Sec. 6.)

[92] C. Morel, et al., Measurement of the inclusive J / psi production cross-sections in anti-p p and p p collisions at s**(1/2) = 24.3-GeV, Phys. Lett. B252 (1990) 505–510, [Conf. Proc.C900802V1,C900802V1:447(1990)]. (Cited in Sec. 8.2.3.1.)

[93] L. Antoniazzi, et al., Production of J / Psi via psi-prime and xi decay in 300-GeV/c proton and pi+- nucleon interactions, Phys. Rev. Lett. 70 (1993) 383–386. (Cited in Sec. 8.2.3.1.)

[94] H. D. Snyder, et al., Production of ψ (3100) and ψ' (3700) in p-Be Collisions at 400-GeV, Phys. Rev. Lett. 36 (1976) 1415. (Cited in Sec. 8.2.3.1.)